nature methods

Article

https://doi.org/10.1038/s41592-026-03079-w

Spatial 5mC-seq profiling of embryos and decidua after implantation in mammals

Received: 1 October 2025

Accepted: 23 March 2026

Published online: 27 April 2026

Check for updates

Xun Shan[1,2,5], Yimin Tang[1,2,5], Jinzhou Hu[1,2], Mingyuan Bian[3], Xuelong Yao[4], Lei Gao[1] ✉ & Jiang Liu[1,2] ✉

DNA methylation is vital for development and diseases, yet no spatial DNA methylation profiling technology has been reported. Here we developed spatial 5mC-seq (SmC-seq), a microfluidic-based method providing unbiased genome-wide methylome at near single-cell resolution. Applying SmC-seq to mouse post-implantation development revealed a clear spatial heterogenous pattern of DNA methylation in inner cell mass-derived tissues. We identified a two-layer organization in the E8.5 ectoplacental cone with distinct methylation and proliferation states. Unexpectedly, a portion of maternal tissue with low DNA methylation level, enriched for nutrient-supplier progenitors, is observed in the middle region of decidua post-implantation. The hypomethylated regions in the nutrient-supplier progenitor cluster are associated with cell proliferation. Notably, the genes associated with hypomethylated regions in mature nutrient-supplier cluster are enriched in exocytosis and nutrient synthesis, linked to nutrient provision for embryogenesis before placental function. In summary, SmC-seq enables spatial DNA methylation mapping, advancing our understanding of biological events.

Spatial epigenomics technologies provide powerful tools to uncover epigenetic heterogeneity, as well as the spatial heterogeneity and organizational architecture of tissues, allowing for a more comprehensive understanding of biological systems[1–4]. DNA methylation is a well-studied epigenetic modification, which regulates gene expression (GE), transposon silencing and genomic stability[5,6]. Recently, single-cell DNA methylation technologies have been developed[7–9]. A limitation of these technologies is their inability to preserve the original spatial coordinates of cells, which obscures how epigenetic heterogeneity is organized and whether DNA methylation also exhibits spatial heterogeneity within tissues. In contrast, spatial DNA methylation technologies enable direct correlation of DNA methylation states with spatial locations and histological features to offer clues to the organizational principles of tissues. However, until now, no spatial DNA methylation profiling methods has been reported.

During early embryogenesis, mammalian zygotes develop into blastocysts, which consist of inner cell mass (ICM) and trophectoderm (TE). After blastocyst implantation into the mother's uterus, both embryo and maternal uterine endometrium undergo extensive changes. In embryos, ICM differentiates into epiblast and primitive endoderm. Epiblast further differentiates into ectoderm, mesoderm and endoderm, which collectively form the fetus, while primitive endoderm differentiates into visceral endoderm (VE) and parietal endoderm[10]. Meanwhile, the TE cells consist of polar TE directly contacting with ICM, and mural TE surrounding the blastocoel. After implantation, the mural TE differentiates into primary trophoblast giant cells (TGCs), while polar TE forms the extra-embryonic ectoderm (ExE) and the ectoplacental cone (EPC)[10]. The EPC appears as a triangle cap extending into the mesometrial decidua. After gastrulation, the EPC and chorionic cavities are formed, with the base of EPC cavity and extra-embryonic mesoderm forming the chorion plate[10]. In mouse embryonic day 8.5 (E8.5) embryo, fusion of the chorion plate and allantois initiates hemochorial placentation[11]. Chorionic trophoblast precursors then differentiate into multinucleated syncytiotrophoblast cells through

[1]State Key Laboratory of Epigenetic Regulation and Intervention, CAS Center for Excellence in Biomacromolecules, Institute of Biophysics, Chinese Academy of Sciences, Beijing, China. [2]University of Chinese Academy of Sciences, Beijing, China. [3]School of Mathematical Science, Peking University, Beijing, China. [4]Guangzhou Nvwa Life Technology Co., Guangzhou, China. [5]These authors contributed equally: Xun Shan, Yimin Tang. ✉e-mail: gaol@ibp.ac.cn; liujiang@ibp.ac.cn

cell–cell fusion, and mononucleated sinusoid TGCs[12]. Together with endothelial cells, they constitute the maternal–fetal interface of the labyrinth zone[12,13]. As vascular networks expand, EPC-derived cells form the spongiotrophoblast layer containing spongiotrophoblast cells, glycogen trophoblast cells and several TGC types. This layer, along with the secondary parietal-TGC layer, defines the junctional zone[11,12]. The labyrinth and junctional zone together constitute the major layers of the definitive placenta that can eventually mediates nutrients and oxygen exchange between mother and fetus. Alongside embryo implantation, maternal uterine tissue undergoes decidualization to support the further development of embryo. Extensive cell fate determinations and transitions occur during this process[11,14].

The mammalian embryos undergo de novo DNA methylation after implantation[9], which is critical for germ layer cell fate determination[15]. In contrast, TE continues to exhibit low methylation levels (MLs), which may potentially promote the invasiveness of trophoblast cells[16]. Previous studies using gene-editing cell lines and animal models have demonstrated the essential role of DNA methylation in the normal development and function of the trophoblast lineage[17,18]. For example, the loss of DNA methyltransferase Dnmt3b led to the activation of germline genes in trophoblast cells and impaired the formation of the maternal–fetal interface[19]. Furthermore, growing evidence suggests that abnormal DNA methylation is associated with the development of preeclampsia, a disorder linked to placental dysfunction[16]. Although previous single-cell DNA methylation analyses have explored embryonic tissues, such as epiblast, ectoderm, mesoderm and endoderm[9], single-cell DNA methylation dynamics of TE during post-implantation development remain largely unexplored in vivo. In addition, previous study reported a stable DNA methylation status during decidualization in induced human endometrial stromal cells in vitro[20]. However, the dynamics of DNA methylation during decidualization in vivo are still unknown.

In addition, due to the lack of spatial DNA methylation method, the spatial characteristics of DNA methylation during embryonic development after implantation remain unexplored. In this study, we aim to establish a spatial 5mC-seq method and investigate the spatiotemporal dynamics of DNA methylation in embryonic and decidual cells (DCs) after implantation.

Result

The workflow of SmC-seq

To develop a spatial 5mC-seq method (SmC-seq), we utilized a microfluidic system (Extended Data Fig. 1a) to capture DNA methylome while simultaneously preserving the spatial location information of cells in tissue (Fig. 1a). A frozen tissue section is fixed with formaldehyde to retain its structural integrity. Because genomic DNA is wrapped around histone octamers, which impedes the fragmentation for DNA methylation library preparation, tissue section was treated with three rounds of hydrochloric acid solution to remove histones from chromatin (Methods). This step is crucial to enhance the genomic coverage of SmC-seq (Extended Data Fig. 1b). We also checked the diffusion pattern of our chip, showing no cross-channel contamination (Extended Data Fig. 1c,d). Following histone removal, Tn5 transposition is performed to fragment the genomic DNA and add adaptors containing a ligation linker. Two rounds of ligation reactions are then conducted using microfluidic chips with microchannels to introduce 11-mer barcodes A and B to the DNA fragment ends. The unique combination of barcodes A and B encodes the spatial positions of cells within the tissue. As cytosine undergoes conversion to uracil during 5mC library construction, cytosine is excluded from barcodes. The DNA fragments are then reverse cross-linked and purified for subsequent DNA methylation library preparation.

Gap filling and DNA extension are performed using a dNTP mixture containing 5-hydroxy-deoxycytidine triphosphate (5-hydroxy-dCTP) instead of dCTP, which protects cytosines in the inserted sequences from deamination in the following steps. Next, an enzymatic methyl-seq procedure is employed to construct DNA methylation sequencing library[21]. During this process, TET2 and a β-glucosyltransferase (β-GT) are used to convert 5mC to 5-carboxycytosine (5caC) or glycosylated 5hmC (5ghmC), then apolipoprotein B mRNA-editing enzyme catalytic polypeptide-like (APOBEC) protein is used to deaminate unmethylated cytosines to uracils. Finally, the libraries are PCR amplified for sequencing, in which unmethylated cytosines are recognized as thymines while methylated cytosines remain as cytosines. Our method is based on enzymatic methyl-seq, which cannot distinguish 5mC from 5hmC. Our SmC-seq data represents a combined 5mC/5hmC signal.

To evaluate the feasibility of our SmC-seq method, we applied it to profile DNA methylation patterns in a mouse E5.5 embryo section embedded within the maternal decidual tissue (Fig. 1b). Microfluidic chips with microchannels (10 μm in width per channel) were used for the experiment. The data quality was systematically assessed. The SmC-seq data show high enzymatic conversion rates, with 98.6% glycosylation protection and 98.0% deamination efficiency (Supplementary Table 1). Our data show a uniform distribution of sequencing reads across the tissue (Fig. 1c). The genome coverage of a single pixel can reach up to 3.46% (Supplementary Table 2). The average number of cytosine–phosphate–guanine dinucleotides (CpGs) detected per pixel was 230,561 covering 1.05% of CpGs across the whole genome. We find that accumulating about 200 pixels can reach the genomic coverage threshold (80% of mouse genome) (Extended Data Fig. 2a). Moreover, the sequencing reads are evenly distributed across the chromosomes and randomly distributed in different genomic elements (Extended Data Fig. 2b,c), suggesting no genomic region bias in the SmC-seq data. Analyses of our SmC data show that the global DNA ML of E5.5 embryos is around 0.61 (Fig. 1d and Extended Data Fig. 2d), which is consistent from the ML of E5.5 embryo analyzed from previous studies[9,22] (Extended Data Fig. 2d). To benchmark the coverage of CpGs across the genome, we compared our data with four published single-cell DNA methylation sequencing datasets, generated by scNMT-seq, sci-Cabernet, snmC-seq2 and sciMETv2, respectively[7,9,23,24]. As genome coverage positively correlates with sequencing depth, we normalized genome coverage by sequencing depth for each pixel, referred to as standardized coverage. Our results show that our method is comparable with published methods (Fig. 1e). Further scatter-plot analyses of methylation signals across genomic regions (10 kb, 100 kb and 1 Mb binning) show good correlation between our SmC-seq data with two public datasets (Extended Data Fig. 2e). These results suggest that our SmC-seq method achieves high capture efficiency for whole-genome DNA methylation analysis.

To further examine the DNA methylation pattern at the pixel level detected by SmC-seq, we profiled DNA methylation in mouse E7.5 embryos and compared the data with published single-cell and bulk DNA methylation datasets of mouse embryos at the corresponding developmental stage[9,15]. The spatial patterns of DNA MLs in E7.5 embryo sections were consistent across two biological replicates (Fig. 1f and Extended Data Fig. 3a–c). The methylation states of about 80% of 1 kb bins are similar to the previous published datasets[9,15] (Extended Data Fig. 3d–f). These data indicate that our SmC-seq method is robust. Our data also show that DNA MLs are high in the pixels of epiblast-derived cells (EDCs), but low in those of extra-embryonic cells (EXCs), which include TE-derived cells and primitive endoderm-derived cells (Fig. 1f and Extended Data Fig. 3g). We further integrated our spatial DNA methylation data with a published single-cell DNA methylation dataset and performed clustering analysis based on DNA methylation patterns of genomic regions (Methods). The uniform manifold approximation and projection (UMAP) clustering results show that these pixels can be divided into two major groups (Fig. 1g), which are annotated as the EDC cluster and the EXC cluster based on their spatial location in the mouse embryo (Fig. 1h). Consistently, the promoter MLs of known embryonic cell marker genes, such as

https://doi.org/10.1038/s41592-026-03079-w

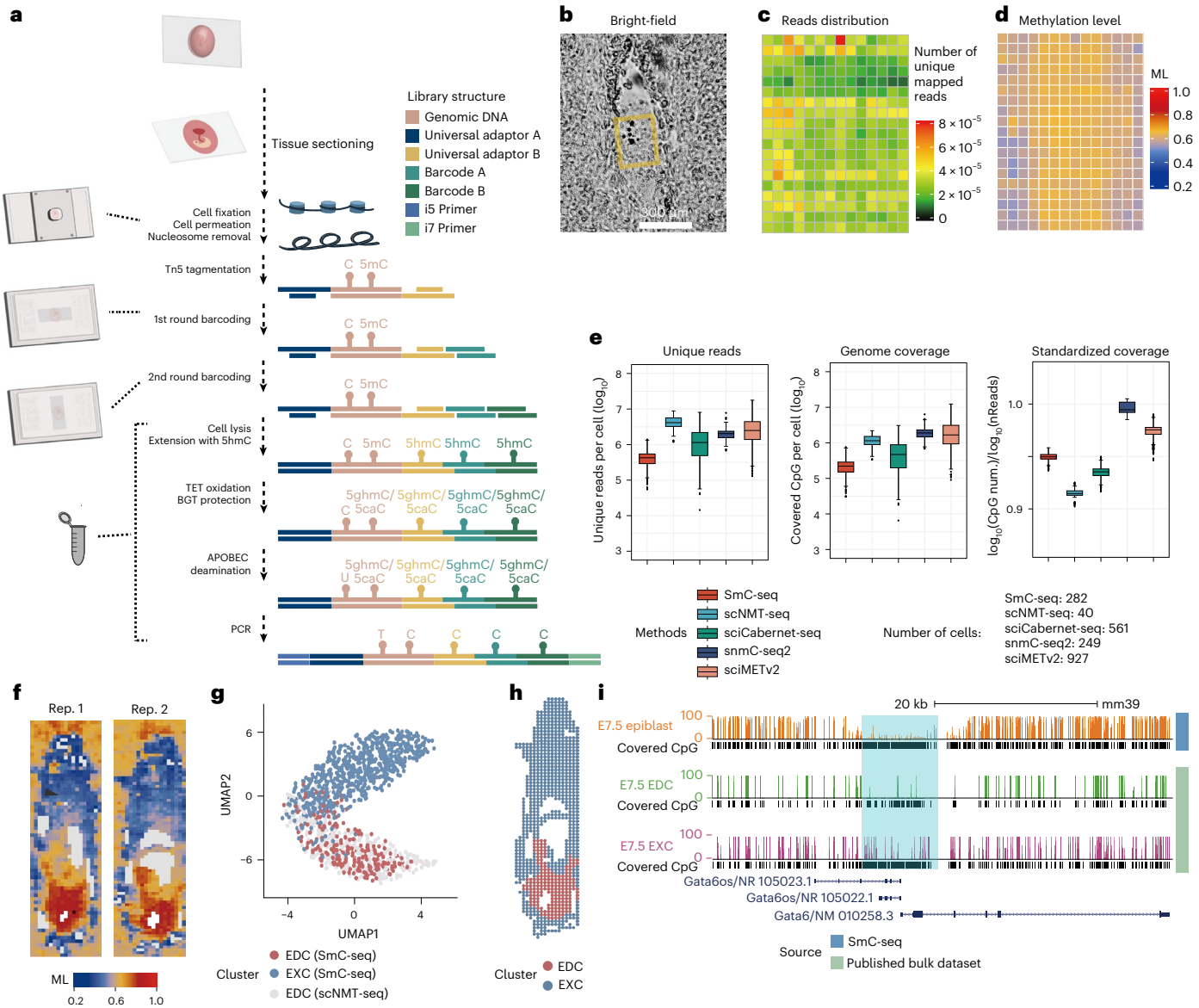

Fig. 1 | Establishment and quality assessment of spatial 5mC-seq method. **a**, The workflow of SmC-seq. **b**, Bright-field image of mouse embryo-maternal tissue at the E5.5 stage. The yellow rectangle marks the embryonic region in the tissue used for SmC-seq. This experiment was performed once for benchmarking. **c**, Spatial distribution of the number of unique mapped reads from SmC-seq data for the mouse E5.5 embryo shown in **b**. Each pixel represents a 10 × 10-μm region. Fluidic chips with 10-μm-width microchannels and 5-μm-interval chips were used for this analysis, with the interval walls between fluid channels omitted in the figure. **d**, Spatial distribution of 5mC levels of the mouse E5.5 embryo. Global DNA ML for each pixel was calculated. **e**, Box plots comparing the number of unique mapped reads (left), genome coverage (middle) and standardized genome coverage (right) among the DNA methylation sequencing data obtained using five different methods, including the SmC-seq developed in this study (10 × 10-μm resolution) and four published single-cell DNA methylation sequencing methods (scNMT-seq, sci-Cabernet, snmC-seq2, and sciMETv2). The numbers of pixels or cells used for comparison among these methods are shown at the bottom. The box indicates the interquartile range (IQR; 25th–75th percentiles), the center line denotes the median, and whiskers extend within 1.5 × IQR. Points beyond the whiskers are shown as outliers (circles). **f**, Spatial distribution of 5mC levels of two replicates of mouse E7.5 embryos. Rep., replicate. Each pixel represents a 10 × 10-μm region. The asterisks mark the embryos, while the arrowheads mark the extra-embryonic tissues. Fluidic chips with 10-μm-width microchannels and 5-μm-interval chips are used for this analysis. **g**, UMAP visualization of blastocyst-derived pixels based on the SmC-seq data from the E7.5 embryo (rep. 2) in **f**. Single-cell DNA methylation data from EDCs generated by scNMT-seq were incorporated for comparison. The pixels from SmC-seq data were classified into two clusters, including EDCs and EXCs. **h**, Spatial distribution of the EDC and EXC clusters in the E7.5 embryo. **i**, Genome browser view of DNA MLs at the *Gata6* locus in EDC and EXC clusters measured by SmC-seq, and in E7.5 embryo from published bulk whole genome bisulfite sequencing data (Li et al.[15]). The cyan shaded region highlights a DMR located in the *Gata6* promoter. The MLs of the highlighted region in epiblast, EDC and EXC are 0.011, 0.031 and 0.072, respectively.

Pou5f1 and *Tdgf1*, are low in the EDC cluster but high in the EXC cluster (Extended Data Fig. 3h,i). Furthermore, the EDCs in the published single-cell data largely overlap with the annotated EDCs in our dataset, but do not overlap with the EXCs of our spatial data (Fig. 1g). We also compared the pseudobulk 5mC signal from our SmC-seq data with published single-cell and bulk DNA methylation datasets for mouse E7.5 embryos[9,15]. Our data have a good correlation with the public data (Extended Data Fig. 3j,k). A representative example is shown in Fig. 1i. In summary, the SmC-seq method is robust, and reveals a clear spatial pattern of DNA methylation in the implanted embryos.

https://doi.org/10.1038/s41592-026-03079-w

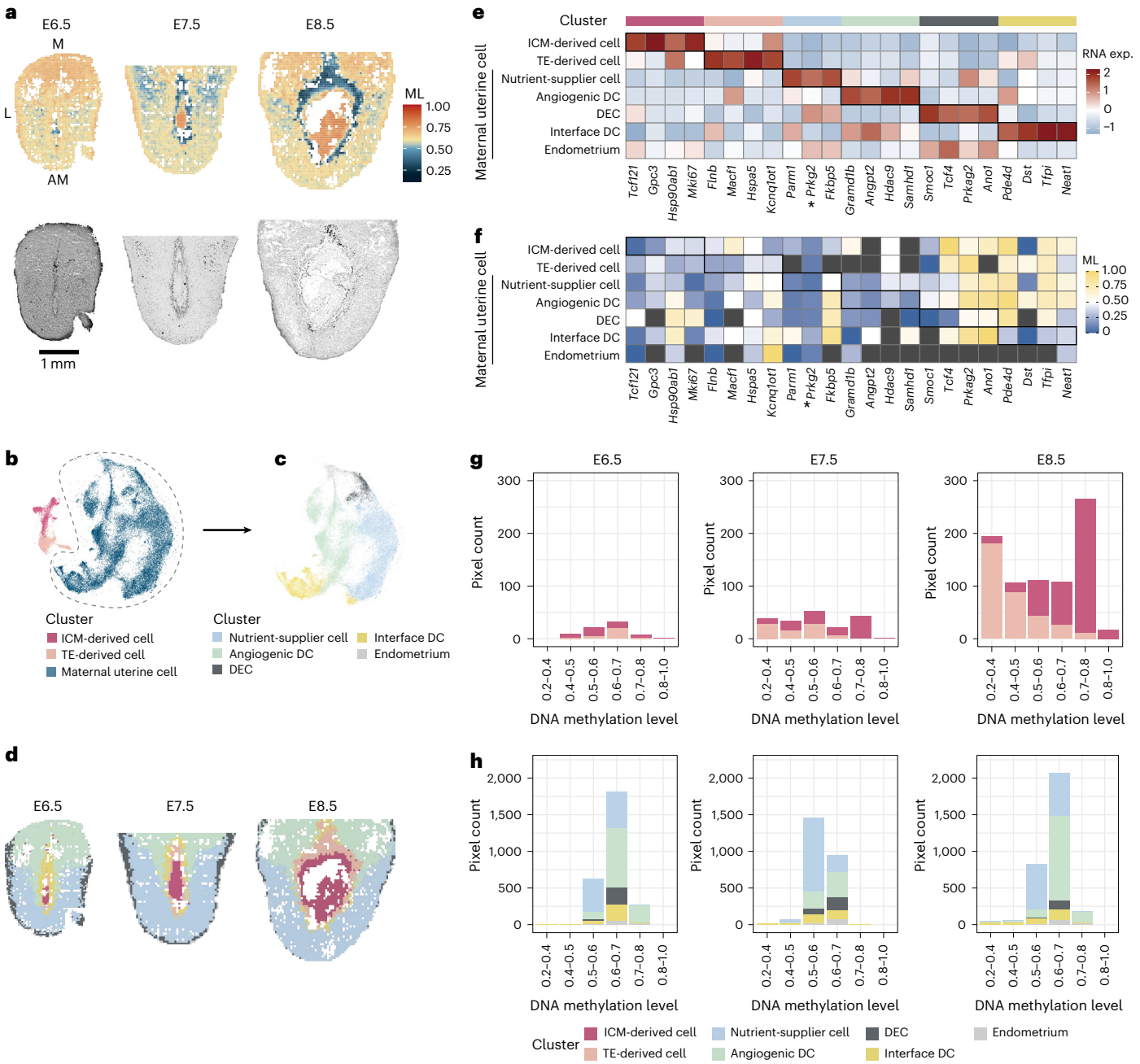

Fig. 2 | Spatial mapping and dynamics of DNA MLs in embryo-maternal tissues after implantation. a, Top: spatial distribution of DNA MLs of mouse embryo-maternal tissues after implantation at the E6.5 (left), E7.5 (middle) and E8.5 (right) stages. Fluidic chips with 20-μm-width microchannels were used in this analysis. Each pixel represents a 20 × 20-μm region, with the interval walls between fluid channels omitted in the figure. M, mesometrial; AM, antimesometrial; L, lateral. Bottom: the bright-field image of the corresponding sections. **b**,**c**, UMAP visualization of clustering result based on spatial RNA-seq data from tissue sections adjacent to those used for SmC-seq in **a**. Three major clusters (**b**). Refined clustering of the maternal uterine tissue identified in **b** (**c**). DEC, decidual endometrial cell. **d**, Spatial distribution of different clusters in mouse embryo-maternal tissues after implantation at the E6.5 (left), E7.5 (middle) and E8.5 (right) stages. Fluidic chips with 20-μm-width microchannels were used in this analysis. Each pixel represents a 20 × 20-μm region, with the interval walls between fluid channels omitted in the figure. The annotations of clusters are shown in **b** and **c**. **e**, Heatmap showing RNA expression levels of cell-type-specific marker genes across different clusters, classified using spatial RNA-seq data. **f**, Heatmap showing DNA MLs of the promoters of cell-type-specific marker genes across different clusters, based on the integrated spatial RNA-seq and SmC-seq data. In **e** and **f**, the asterisk (*) highlights a marker gene associated with decidualization. **g**,**h**, Bar plots showing the numbers of pixels in different clusters within various DNA ML ranges at different developmental stages. For example, DNA MLs of pixels in nutrient-supplier cell cluster are usually in the window of 0.5–0.6 or 0.6–0.7, whereas the MLs of most of pixels in TE-derived cell cluster are in the window of 0.2–0.4 or 0.4–0.5. The results of embryo-derived clusters and maternal uterine tissue-derived clusters are shown in **g** and **h**, respectively.

Embryonic and maternal uterine tissues exhibit distinct dynamic patterns of DNA methylation after implantation

To examine the spatiotemporal dynamics of DNA methylation after implantation, we collected mouse tissues containing both conceptus and maternal uterine tissues from the E6.5 to E8.5 stages to perform SmC-seq (Fig. 2a). Genome coverage scales with sequencing depth across datasets (Extended Data Fig. 4a,b). The 20-μm-wide microchannel chips were used to ensure effective coverage of both embryonic and maternal uterine tissue components for the spatial profiling of DNA methylation. Notably, DNA MLs vary across the tissue (Fig. 2a).

Unlike the high DNA MLs in mature somatic cells, a substantial portion of maternal decidua cells in the middle region of lateral decidua exhibit low DNA MLs, especially at the E7.5 stage (ML <0.65) (Fig. 2a). To validate this result, we used immunofluorescent staining to examine the methylation signal in decidua. The staining results show that DNA methylation signals of some decidua cells in the middle region of lateral decidua are low at the E7.5 stage (Extended Data Fig. 4c), suggesting that DNA methylation of decidua may undergo demethylation after embryonic implantation. To exclude the possibility that low ML may be resulted by high proliferation, we performed co-immunostaining for 5mC and Mki67. Mki67 is a marker for replicating cells[25]. Our results show that many cells with low 5mC level show no or low Mki67 expression (Extended Data Fig. 4d). Furthermore, DNA methylation signals between $Mki67^{+}$ and $Mki67^{-}$ cells are comparable (Extended Data Fig. 4e). These results suggest that lowly methylated cells are not caused by cell proliferation. Our result is different from the previous report that DNA methylation remains stable during decidualization in human endometrial stromal cells under in vitro conditions[20].

To better characterize the cellular identities, we collected the adjacent tissue slides for spatial RNA-seq analysis, assuming that neighboring tissue slides would have similar cell compositions and spatial distribution patterns. Overall, the median number of expressed genes per pixel in a tissue section is around 1,000 (Extended Data Fig. 4f,g). Based on the spatial RNA-seq data, all pixels can be categorized into three major clusters: ICM-derived cell cluster, TE-derived cell cluster and maternal uterine cell cluster (Fig. 2b). The marker used in identifying these clusters can be found in Supplementary Table 3. Moreover, the maternal uterine cluster can be further clustered into five subclusters: endometrium, decidual endometrial cells, angiogenic DCs, nutrient-supplier cells and interface DCs (Fig. 2c,d and Extended Data Fig. 4h). The ICM-derived cell cluster is characterized by elevated expression levels of *Gpc3* (Fig. 2e), which encodes a membrane-bound heparin sulfate proteoglycan that functions in embryonic cell growth and differentiation[26]. TE-derived cell cluster is characterized by a trophoblast cell marker *Flnb* (Fig. 2e), which encodes Filamin B[27]. Maternal uterine cell cluster exhibits high expression level of *Prkg2* (Fig. 2e), which encodes type II cGMP-dependent protein kinase, a key regulator of decidualization[28]. The distribution of these clusters within the maternal-conceptus tissue (Fig. 2d) aligns with previous hematoxylin and eosin staining results[29]. Furthermore, among maternal uterine cell subclusters, the angiogenic DC cluster exhibits high expression of *Angpt2* (Fig. 2e), a well-known growth factor governing endothelial cell behavior and vascular remodeling[30]. The nutrient-supplier cell cluster is characterized by the active expression of several metabolism-associated genes[31], including *Fkbp5* (also known as *Fkbp51*) (Fig. 2e).

Next, we integrated the RNA-seq-based clusters with the SmC-seq data based on tissue outlines (Extended Data Fig. 5a,b and Methods), and assessed DNA MLs across different clusters within the entire tissue. In genome-wide level, GE shows negative correlation with promoter ML and positive correlation with gene body ML (Extended Data Fig. 6a,b). For example, a negative correlation between expression levels of some marker genes and their promoter MLs (Fig. 2e,f).

Then, we compared the global DNA MLs, defined as the average across all CpG sites detected within each pixel (Methods), across different clusters. DNA MLs differ significantly among different clusters (Fig. 2g,h and Extended Data Fig. 7a). For example, the DNA MLs of pixels in nutrient-supplier cell cluster are usually in the range 0.5–0.6 or 0.6–0.7 (Fig. 2h), whereas the MLs of most of pixels in TE-derived cell cluster are in the range 0.2–0.4 or 0.4–0.5 (Fig. 2g).

We further investigated the dynamics of DNA MLs of pixels in the ICM-derived cell cluster and TE-derived cell cluster during development. The DNA MLs of pixels in ICM-derived cell cluster gradually increase from the E6.5 to E8.5 stage (Extended Data Fig. 7b). In contrast, the DNA MLs of pixels in TE-derived cell cluster decrease at the E7.5 stage and further decline at the E8.5 stage (Extended Data Fig. 7c). The decrease trend of DNA methylation in TE is further confirmed by our immunofluorescence staining (Extended Data Fig. 7d,e).

Collectively, the DNA methylation dynamics of maternal uterine and conceptus cells exhibit distinct spatial and temporal patterns at genome-wide level during post-implantation development.

Dynamics of DNA methylation in ICM-derived tissues

Next, we explored the spatiotemporal dynamics of DNA methylation of pixels in the tissue derived from ICM from the E5.5 to E7.5 stages (Fig. 3a). The examined pixels can be categorized into three clusters based on the spatial DNA methylation data (Fig.3b and Extended Data Fig. 8a–c). Based on their position within the tissues (Fig. 3b and Extended Data Fig. 8d) and the promoter DNA MLs of various cell type marker genes (Fig. 3c), these three clusters were annotated. Clusters 1, 2 and 3 are enriched for epiblast, extra-embryonic endoderm (ExEndo; including visceral and parietal endoderm) and extra-embryonic visceral layer (ExVL; including extra-embryonic mesoderm and extra-embryonic VE), respectively. At the genome-wide level, GE shows negative correlation with promoter ML and positive correlation with gene body ML (Extended Data Fig. 8e–i). For example, *Ctrc* is highly methylated in promoter and shows no expression in E7.5 embryo (Extended Data Fig. 8g). Moreover, the epiblast marker gene *Pou5f1* exhibits lower methylation on its promoter in cluster 1 (Fig. 3c), which contains an epiblast cavity[32]. Similarly, the VE marker gene *P4ha2* shows exclusive promoter hypomethylation in cluster 2 (Fig. 3c), which resides in the distal part of conceptus[33]. Yolk sac endoderm-related gene *Ttr*[34] and yolk sac mesoderm-related gene *Cd59a*[35] exhibit promoter hypomethylation and high expression levels in cluster 3 (Fig. 3c). At the E6.5 and E7.5 stages, the DNA MLs of cluster 1, which contains three germ layers, do not show notable regional heterogeneity (Fig. 3a,b), indicating that the DNA MLs are similar among the cells of the three germ layers. Consistent with previous knowledge[22], the DNA MLs of the pixels in cluster 1 (epiblast) increase from the E5.5 to E6.5 stage and then remain relatively stable (Extended Data Fig. 9a).

Then, we analyzed the differentially methylated regions (DMRs) of the cluster 1 (epiblast) at the E5.5, E6.5 and E7.5 stages. In this study, the DMRs analyses are focused on promoters and enhancers[36]. We identified 6,307 hypermethylated DMRs (hyperDMRs) and 2,276 hypomethylated DMRs (hypoDMRs) in E6.5 embryos compared to E5.5 embryos (Fig. 3d). We identified 1,464 hyperDMRs and 1,198 hypoDMRs in the E7.5 embryos compared to E6.5 embryos (Fig. 3e). We also compared the DMRs to a previously published scNMT-seq dataset of mouse early embryo during the onset of gastrulation[9]. It shows that about 28–47% of DMRs identified by our data are confirmed by scNMT-seq data (Extended Data Fig. 9b). Gene Ontology (GO) analyses show that genes associated with hypoDMRs at the E6.5 stage are enriched in the regulation of somitogenesis (Fig. 3d), exemplified by *Cdx1* (ref. 37) (Fig. 3f), consistent with the determination of somitic cell fate occurring as early as the E6.5 stage. The genes associated with hyperDMRs at the E6.5 stage are enriched in the anterior–posterior axis specification (Fig. 3d), exemplified by *Otx2* (Fig. 3f), consistent with the finding that *Otx2* functions in the anterior–posterior axis specification[38]. We also observed that the genes associated with hypoDMRs at the E7.5 stage, compared to the E6.5 stage, are enriched in negative regulation of cell migration (Extended Data Fig. 9c), exemplified by *Arap3* (ref. 39) (Extended Data Fig. 9d).

Compared to the epiblast cluster, DNA MLs are much lower in extra-embryonic tissues (clusters 2 and 3) (Extended Data Fig. 9e). These two extra-embryonic clusters occupy distinct anatomical regions at the E7.5 stage. Cluster 2 is found adjacent to the distal region of conceptus, whereas cluster 3 occupies the proximal region (Fig. 3b). We sought to explore the differences in DNA methylation patterns between these two clusters, as well as the potential impact of DNA methylation on development. The DNA MLs of pixels in cluster 3 are significantly

https://doi.org/10.1038/s41592-026-03079-w

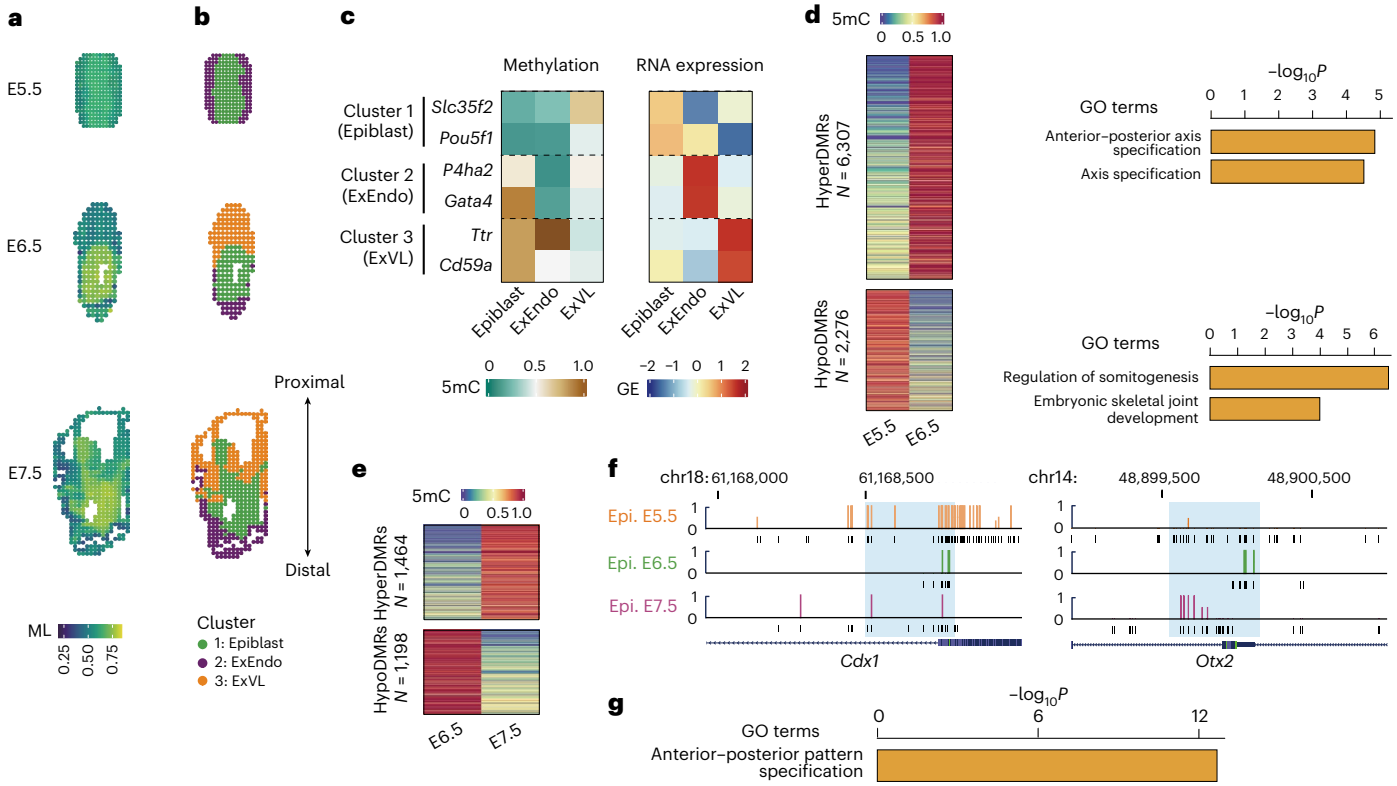

Fig. 3 | Spatial mapping and characterization of DNA methylation of ICM-derived cells in mouse embryos after implantation. a, Spatial distribution of DNA MLs of pixels within ICM-derived cells in mouse embryos at the E5.5 (top), E6.5 (middle) and E7.5 (bottom) stages. Fluidic chips with 10-μm-wide microchannels were used to generate these data. Each pixel represents a 10 × 10-μm region, with the interval walls between fluid channels omitted in the figure. Five-μm-interval chips are used for embryos at E5.5 and E7.5 stages in this analysis. **b**, Spatial distribution of clusters of ICM-derived cells in mouse embryos, based on SmC-seq data. **c**, Heatmap showing promoter DNA MLs and RNA expression levels of cell-type-specific marker genes across different clusters based on SmC-seq and spatial RNA-seq data, respectively. The clusters shown in the left part are classified based on SmC-seq data. The clusters shown in the right part are classified based on spatial RNA-seq data. 5mC, DNA ML of CpG sites. **d**, DNA MLs of DMRs in cluster 1 (epiblast) between the E5.5 and E6.5 stages, and GO enrichment of the genes associated with these DMRs. *N* denotes the number of DMRs. **e**, Heatmap showing DNA MLs of DMRs in cluster 1 (epiblast) between the E6.5 and E7.5 stages. **f**, Genome browser view of DNA MLs at the *Cdx1* and *Otx2* loci in cluster 1 (epiblast) at different developmental stages. Light blue shadows mark the regions of DMRs. The CpG sites covered in SmC-seq data are shown below each signal track. The MLs of the highlighted region in *Cdx1* locus at the E5.5, E6.5 and E7.5 stages are 0.865, 0.375 and 0.154, respectively; the MLs of the highlighted region in *Otx2* locus at the E5.5, E6.5 and E7.5 stages are 0.023, 0.412 and 0.182, respectively. **g**, GO enrichment of the genes associated with hypoDMRs in cluster 2 (ExEndo) compared to cluster 3 (ExVL) at the E7.5 stage.

higher than those in cluster 2 at the E7.5 stage (Extended Data Fig. 9e). We identified 4,479 DMRs that are hypomethylated in cluster 3, and 11,405 DMRs that are hypomethylated in cluster 2. The genes associated with hypoDMRs in cluster 2 are enriched in anterior–posterior pattern specification (Fig. 3g). Given that VE is enriched in cluster 2, this result is consistent with the role of VE in the determination of the anterior–posterior polarity of embryos[40].

DNA methylation dynamics in maternal uterus during post-implantation development

We classified all examined cells into three major groups: ICM-derived cells, TE-derived cells and maternal uterine cells (Fig. 2a,b,d). In this section, we focused on the analyses of maternal uterine cells, whose methylation dynamics remain largely unknown. To address this, we explored the spatial pattern of DNA methylation in mouse maternal uterus tissues surrounding implanted embryos from the E6.5 to E8.5 stages (Fig. 4a). The pixels of maternal uterine tissue can be classified into nine clusters based on DNA methylation patterns (Extended Data Fig. 10a), which show distinct regional distribution within the uterine tissue (Fig. 4b). Clusters M1 and M2 show low ML, which are located in the lateral regions of decidua (Fig. 4a,b and Extended Data Fig. 10b). To further annotate these clusters, we analyzed the spatial RNA-seq data of uterine cells and classified them into nine clusters (Fig. 4c and Extended Data Fig. 10c). The figures illustrate that most cells, including nutrient-supplier-related cells, belong to stromal cells (Extended Data Fig. 10c), as they express common stromal cell marker gene *vimentin*. Our staining data show that most DCs are indeed stromal cells (Extended Data Fig. 4c). Through image alignment of adjacent slides, clusters M6 and M5 include the pixels in endometrium and decidual endometrial cell clusters, cluster M1 is enriched for pixels in the nutrient-supplier progenitor cell cluster and cluster M4 is enriched for pixels in the mature nutrient-supplier cell cluster. Clusters M7 and M9 are enriched for pixels in proliferative angiogenic decidual stromal cell (DSC) and mature angiogenic DSC clusters, respectively. We then performed RNA velocity and pseudotime analyses for maternal decidual tissue. The results inferred a relationship between the nutrient-supplier progenitor cell cluster and mature nutrient-supplier cell cluster (Extended Data Fig. 10d–g). Notably, cluster M1 enriched for the nutrient-supplier progenitor cell cluster exhibited the lowest DNA MLs compared to the other clusters in maternal uterine tissue, including the mature nutrient-supplier cell cluster enriched in cluster M4 (Extended Data Fig. 10b). This suggests that the extremely low DNA methylation state is a particular epigenetic state of the nutrient-supplier progenitor cell cluster.

To explore the potential impact of the low DNA methylation state in cluster M1, we analyzed the functions of genes associated with the hypoDMRs in cluster M1 compared to clusters M5 and M6. These hypoDMR-associated genes are enriched in pathways

https://doi.org/10.1038/s41592-026-03079-w

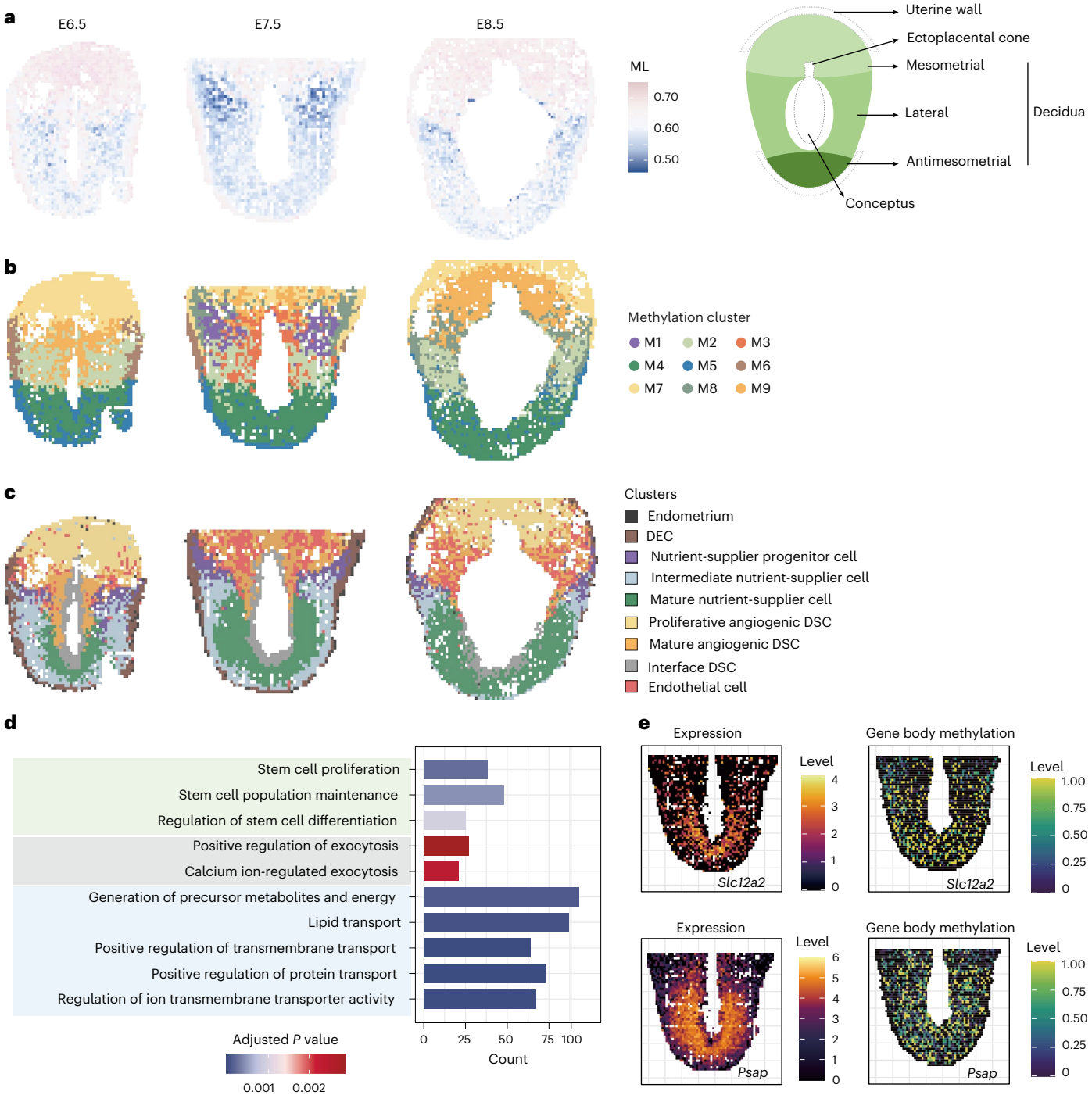

Fig. 4 | Spatial mapping and characterization of DNA methylation of maternal decidual tissue after implantation. a, Spatial mapping of DNA MLs of maternal decidual tissues at the E6.5 (left), E7.5 (middle) and E8.5 (right) stages. Fluidic chips with 20-μm-width microchannels were used to generate the data. Each pixel represents a 20 × 20-μm region. The schematic diagram on the far right illustrates the anatomical structure of the decidua. **b**, Spatial distribution of clusters classified based on SmC-seq data of maternal decidual tissues. **c**, Spatial distribution of clusters classified based on spatial RNA-seq data of maternal decidual tissues. Fluidic chips with 20 μm-width microchannels were used to generate the data. Each pixel represents a 20 × 20-μm region. **d**, GO enrichment of the genes associated with the hypomethylated regions in nutrient-supplier progenitor cell cluster compared to endometrium and DEC clusters at the E7.5 stage. Those hypomethylated regions retain low DNA methylation status in mature nutrient-supplier cell cluster. Hypergeometric test was used in this analysis. **e**, Spatial distribution of RNA expression level (left) and gene body ML (right) of representative marker genes of mature nutrient-supplier cells in mouse maternal uterine tissue at the E7.5 stage.

regulating stem cell proliferation and stem cell population maintenance (Fig. 4d), which is the reason that we annotate this cluster as the nutrient-supplier progenitor cell cluster. Consistently, many Mki67$^+$ cells in the lateral decidua exhibited a low DNA methylation signal (Extended Data Fig. 4d). In addition, Slc25a33, a mitochondrial carrier protein associated with cell growth and proliferation[41], is highly expressed in nutrient-supplier progenitor cells at a transcriptomic level (Supplementary Fig. 1a). Collectively, these data suggest that a low DNA methylation state in nutrient-supplier progenitor cells is associated with cell proliferation.

Given that there is an inferred relationship between the nutrient-supplier progenitor cell cluster and mature nutrient-supplier cell cluster (Extended Data Fig. 10d,e), DNA MLs of pixels in cluster M4 enriched for mature nutrient-supplier cell were significantly higher than those in cluster M1 enriched for nutrient-supplier progenitor cells (Extended Data Fig. 10b). We further conducted GO analysis on genes associated with hyperDMR in cluster M4 compared to cluster M1. These genes are enriched in the processes related to somatic stem cell division and the regulation of cell proliferation (Supplementary Fig. 1b). Consistently, the expression levels of genes associated with the hyperDMRs, such as a stem cell proliferation-related gene *Zbtb16* (ref. 42), were significantly lower in the mature nutrient-supplier cell cluster compared to the nutrient-supplier progenitor cell cluster (Supplementary Fig. 1c). This suggests that the hypermethylation state of mature nutrient-supplier cell is associated with the attenuation of proliferative capacity. Notably, GO analysis of genes associated with genomic regions that maintain low DNA methylation in cluster M4 enriched for mature nutrient-supplier cells compared to cluster M1 show enrichment in positive regulation of exocytosis, regulation of generation of precursor metabolites and energy, lipid transport and positive regulation of protein transport (Fig. 4d). Consistently, lipid transport and carboxylic acid transport are also enriched in the mature nutrient-supplier cell cluster according to the results of GO analyses of genes with specific expression (Supplementary Fig. 1d). For instance, *Slc12a2* (a gene involved in transmembrane transport)[43] (Fig. 4e), *Psap* (a gene involved in lipid metabolism)[44] (Fig. 4e), *Glul* (a gene involved in nitrogen metabolism and amino acid biosynthesis)[45] and *Fabp4* (a gene involved in lipid transport)[46] (Supplementary Fig. 1e) are specifically expressed in the mature nutrient-supplier cell cluster. Furthermore, Psap$^+$ stromal cells are observed in the lateral decidua region, similar to the positioning of mature nutrient-supplier cell cluster near the yolk sac (Supplementary Fig. 1f). In summary, the mature nutrient-supplier cell cluster is associated with the production of various nutrients and exocytosis, suggesting their potential ability to secrete nutrients. Therefore, we designated this cluster as the mature nutrient-supplier cell cluster.

Taken together, the low methylation state of nutrient-supplier progenitor cells is associated not only with their proliferative capacity but also with the nutrient provision process in mature nutrient-supplier cells.

Dynamics of DNA methylation in TE-derived tissue

Finally, we wanted to investigate the dynamics of DNA methylation in TE-derived cells. Placenta is developed from TE. Although the potential impact of DNA methylation during early placental development has been explored, the spatiotemporal dynamics of DNA methylation during early placental development remains unclear. Here, we report the spatial DNA methylation pattern of TE-derived cells at the E8.5 stage (Fig. 5a). We performed cluster analysis based on spatial DNA methylation. Four clusters were classified (Fig. 5b and Supplementary Fig. 2a). In contrast, only two clusters can be classified if there is only DNA methylation data without spatial information (Supplementary Fig. 2b). Notably, clusters 1 and 2 present a clear two-layer pattern (Fig. 5b), with significantly different DNA MLs between these clusters (Supplementary Fig. 2c), which is confirmed by our immunofluorescence staining (Supplementary Fig. 2d–g).

To further characterize the pixel identities of TE-derived tissue, we analyzed spatial RNA-seq data of the slide which is adjacent to the one used for SmC-seq analysis. Three TE-derived clusters are identified, including the inner EPC, outer EPC and parietal-TGCs (Fig. 5c and Supplementary Fig. 3a,b). We then integrated the clusters derived from SmC-seq data with those from spatial RNA-seq data. In genome-wide level, GE shows negative correlation with promoter ML and positive correlation with gene body ML (Supplementary Fig. 3c,d). The promoters of inner EPC marker genes are exclusively unmethylated in cluster 1, while the promoters of outer EPC marker genes are specifically unmethylated in cluster 2 (Fig. 5d). Combined with the spatial information from DNA methylation data (Fig. 5b) and RNA data (Fig. 5c), cell clusters 1 and 2 correspond to inner EPC and outer EPC, respectively. We also observed that spatial context improved the accuracy of cell clustering based on DNA methylation data (Supplementary Fig. 3c,e).

We then sought to explore the relationship and differences between inner and outer EPC clusters. RNA velocity analysis infers that outer EPC originates from inner EPC (Fig. 5e). The DNA ML of the inner EPC cluster is significantly lower than that of the outer EPC cluster (Fig. 5a and Supplementary Fig. 2c). We also performed GO analyses of differentially expressed genes between the inner and outer EPC clusters. Our data show that cell proliferation-related genes are enriched in the inner EPC cluster, whereas genes involved in angiogenesis and protection from natural killer cell-mediated cytotoxicity are enriched in the outer EPC cluster (Supplementary Fig. 3f,g). Additionally, cell proliferation-related genes exhibit higher expression levels in the inner EPC cluster than outer EPC cluster (Supplementary Fig. 3h). Consistently, promoter DNA MLs of these cell proliferation-related genes are much lower in inner EPC cluster than outer EPC (Supplementary Fig. 3i), exemplified by *Cdk5rap2* (Fig. 5f). This result suggests that the inner EPC cluster is proliferative. It is confirmed by Mki67 immunostaining result (Supplementary Fig. 2d,g). Moreover, the genes involved in angiogenesis and protection from natural killer cell-mediated cytotoxicity are highly expressed in outer EPC (Supplementary Fig. 3g). For example, *Igta3* and *Lgals9* have higher expression in outer EPC than inner EPC, which is consistent with the hypomethylation in *Igta3* and *Lgals9* promoters in the outer EPC (Fig. 5f). We also notice that the genes whose promoters retain low DNA MLs in both outer and inner EPCs are enriched in the regulation of endothelial cell migration. Taken together, the DNA methylation dynamics during EPC development is associated with placental angiogenesis and immune tolerance, consistent with the role of EPCs in the invasion of conceptus cells into maternal uterine tissue and the formation of vascular system in placenta[47].

Our data show that the DNA MLs of pixels for both inner EPC and nutrient-supplier progenitor cells are low, with a large number of hypomethylated regions (global ML <0.25) (Fig. 5g). Some of these regions are shared by both clusters (Fig. 5g). Our results indicate that genes with hypomethylated promoters in both inner EPC and nutrient-supplier progenitor cell clusters are enriched in stem cell population maintenance and positive regulation of the cell cycle (Fig. 5h). It suggests that the status of low DNA methylation is important for both EPCs and nutrient-supplier progenitor cells in maintaining their proliferative capabilities. In addition, genes with hypomethylated promoters specific to inner EPC cluster are enriched in GTPase regulator activity (Fig. 5i), whereas genes with hypomethylated promoters specific to nutrient-supplier progenitor cell cluster are enriched in exocytosis and regulation of protein catabolic processes (Fig. 5j), consistent with the previous results (Fig. 4d). Together, these findings highlight that while the DNA methylation pattern of EPC and nutrient-supplier progenitor cells share certain characteristics, they also display notable differences.

In summary, a two-layer spatial DNA methylation pattern, consisting of inner EPC and outer EPC, is observed. Furthermore, DNA methylation in TE-derived tissue is associated with the formation of the placenta.

Discussion

Previously, there was no technology capable of profiling DNA methylation with spatial information. Here, we developed SmC-seq, a powerful platform for profiling the spatial DNA methylation landscape at near single-cell resolution. This method demonstrates robust performance, achieving high coverage of up to 3.46% of the entire genome. In this study, we employed a strategic integration of SmC-seq data with spatial RNA-seq data, enabling the precise identification of spatial dynamics of distinct cell types during development. The SmC-seq method

https://doi.org/10.1038/s41592-026-03079-w

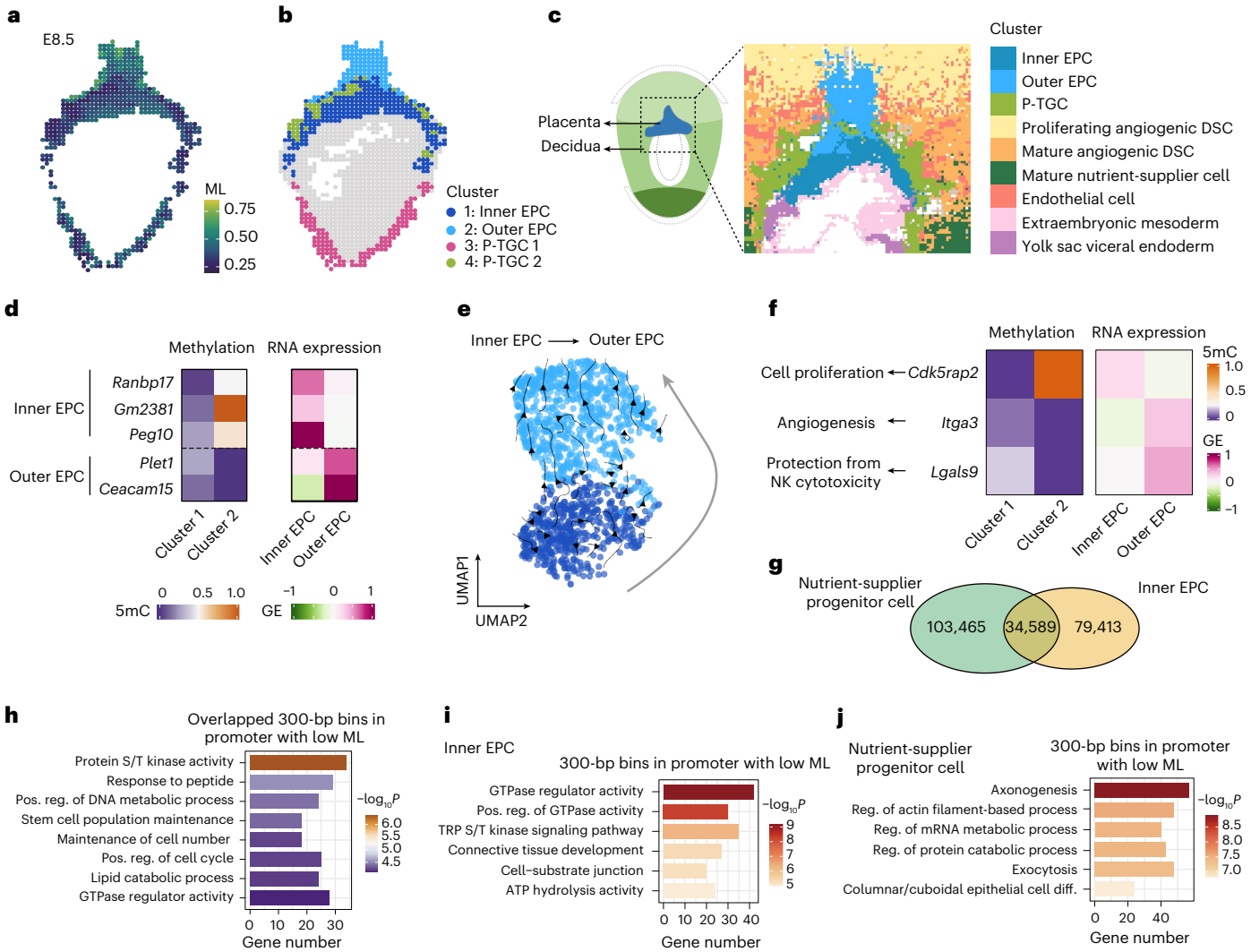

Fig. 5 | Spatial mapping and characterization of DNA methylation of TE-derived cells after implantation. a, Spatial mapping of DNA MLs in mouse extra-embryonic tissue derived from TE at the E8.5 stage. Fluidic chips with 20-μm-wide microchannels were used to generate the data. Each pixel represents a 20 × 20-μm region, with the interval walls between fluid channels omitted in the figure. The global DNA ML of each pixel is shown. **b**, Spatial distribution of clusters classified based on SmC-seq data. P-TGC, parietal-TGC. **c**, Spatial distribution of clusters classified based on spatial RNA-seq data. Fluidic chips with 10-μm-width microchannels were used to generate the data. Each pixel represents a 10 × 10-μm region, with the interval walls between fluid channels omitted in the figure. The dashed rectangle in schematic diagram on the left shows the detected region within the E8.5 decidua. **d**, Heatmap showing promoter DNA MLs and RNA expression levels of marker genes in different clusters based on SmC-seq and spatial RNA-seq data, respectively. Clusters 1 and 2 are classified based on SmC-seq data. Clusters inner EPC and outer EPC are classified based on spatial RNA-seq data. **e**, RNA velocity analysis result of EPC. **f**, Heatmap showing promoter DNA MLs (left) and RNA expression levels (right) of representative genes associated with cell proliferation, angiogenesis and protection from natural killer (NK) cell-mediated cytotoxicity, comparing inner and outer EPCs. **g**, Venn diagram showing the overlap of genomic regions (300-bp bins) with low DNA MLs (ML <0.25) between nutrient-supplier progenitor cell cluster and inner EPC cluster. The numbers of the bins are shown. **h**, GO enrichment analysis of genes with low DNA methylation in their promoters, shared between nutrient-supplier progenitor cell cluster at the E7.5 stage and inner EPC cluster at the E8.5 stage. Two-sided Fisher's exact tests were used in this analysis. **i**,**j**, GO enrichment analysis of genes with promoters that are specifically lowly methylated in inner EPC cluster at the E8.5 stage (**i**) or in nutrient-supplier progenitor cell cluster at the E7.5 stage (**j**). Pos., positive; reg., regulation; diff., differentiation. Two-sided Fisher's exact tests were used in these analyses.

enables us to identify a previously unrecognized two-layered 5mC pattern in the placenta and uncover a spatially ordered 5mC pattern in maternal DCs. Moreover, SmC-seq can reveal spatial heterogeneity of DNA methylation within a single cell cluster. These findings offer new insights into the spatial regulation of DNA methylation during early post-implantation development.

DNA methylation regulates GE and cell differentiation; however, DNA methylation states in many *cis*-regulatory elements are not always consistent with cell differentiation state. DNA methylation states in some *cis*-regulatory elements may be in the prime states before cell differentiation. This may be the reason that the clusters for DNA methylation and RNA expression for decidua cells differ markedly. This discrepancy may also be partly attributable to technical limitations, particularly the sparsity of the methylation signal, which challenges unbiased annotation and dimensionality reduction.

It is worth noting that although using SmC-seq at a 20-μm resolution increases the field of view, it may also obscure some cell-type-specific methylation signatures. In addition, although spatial RNA-seq from an adjacent slide provides a good overview of regional identity, it cannot match methylome and transcriptome profiles on a one-to-one, single-cell basis. This limitation may affect the application of this method in highly heterogeneous tissues.

Before placental function is established, mammalian embryos rely on histotrophic nutrient supply from maternal tissues; however, it remains poorly understood about how yolk sac is formed during mammalian embryogenesis. Our findings suggest that maternal nutrient-supplier cells in the decidua may contribute to this process. Demethylated regions in these cells are enriched for genes involved in nutrient metabolism and exocytosis, accompanied by corresponding transcriptional changes, consistent with a role in nutrient production and secretion. Notably, these cells emerge during yolk sac formation and disappear before the placenta becomes fully functional, suggesting a transient role in supporting embryonic nutrition. Together, these observations raise the possibility that epigenetic remodeling helps coordinate proliferation and functional maturation of maternal nutrient-supplier cells that provide nutrients to the embryo via the yolk sac. Additional experimental validation will be required to confirm this speculation in the future. Our analysis also suggests that spatial variation in DNA methylation may contribute to functional specialization within placental lineages, as reflected by the distinct methylation landscapes observed across EPC layers.

It is also important to consider that global hypomethylation in highly proliferative cell populations may be partly attributable to the delay in restoring symmetrical DNA methylation after replication. In HeLa cells, daughter DNA restored ~80% of parental methylation patterns within 30 min, ~90% within 2 h, and nearly 100% within 10 h of replication, despite a 22-h cell cycle[48]. This suggests that DNA methylation is efficiently preserved within a short time window during cell proliferation, and that cell division alone is unlikely to cause a dramatic reduction in methylation at the cell-population level; however, considering that the maintenance methylation machinery requires several hours to fully remethylate nascent DNA strands[49,50], rapidly cycling cells, such as inner EPCs or nutrient-supplier progenitors, may display a partial loss of reduced global MLs even in the absence of active demethylation. This replication-coupled dilution should be taken into account when interpreting methylation patterns in proliferative tissues.

SmC-seq enables the direct identification of regional heterogeneity within tissues. This capability is critical for unraveling the intricate spatial dynamics of DNA methylation, offering new insights into tissue architecture and its underlying regulatory mechanisms. The versatility of this technology makes it applicable to a wide range of biological contexts and pathologies, and help our understanding of epigenetic regulation in both health and disease.

Online content

Any methods, additional references, Nature Portfolio reporting summaries, source data, extended data, supplementary information, acknowledgements, peer review information; details of author contributions and competing interests; and statements of data and code availability are available at https://doi.org/10.1038/s41592-026-03079-w.

References

1. Zhang, D. et al. Spatial epigenome-transcriptome co-profiling of mammalian tissues. *Nature* **616**, 113–122 (2023).
2. Lu, T., Ang, C. E. & Zhuang, X. Spatially resolved epigenomic profiling of single cells in complex tissues. *Cell* **185**, 4448–4464. e17 (2022).
3. Deng, Y. et al. Spatial profiling of chromatin accessibility in mouse and human tissues. *Nature* **609**, 375–383 (2022).
4. Deng, Y. et al. Spatial-CUT&Tag: spatially resolved chromatin modification profiling at the cellular level. *Science* **375**, 681–686 (2022).
5. Luo, C., Hajkova, P. & Ecker, J. R. Dynamic DNA methylation: in the right place at the right time. *Science* **361**, 1336–1340 (2018).
6. Schubeler, D. Function and information content of DNA methylation. *Nature* **517**, 321–326 (2015).
7. Cao, Y. et al. Single-cell bisulfite-free 5mC and 5hmC sequencing with high sensitivity and scalability. *Proc. Natl Acad. Sci. USA* **120**, e2310367120 (2023).
8. Fabyanic, E. B. et al. Joint single-cell profiling resolves 5mC and 5hmC and reveals their distinct gene regulatory effects. *Nat. Biotechnol.* https://doi.org/10.1038/s41587-023-01909-2 (2023).
9. Argelaguet, R. et al. Multi-omics profiling of mouse gastrulation at single-cell resolution. *Nature* **576**, 487–491 (2019).
10. Thowfeequ, S., Hanna, C. W. & Srinivas, S. Origin, fate and function of extraembryonic tissues during mammalian development. *Nat. Rev. Mol. Cell Biol.* **26**, 255–275 (2025).
11. Jiang, X. et al. A differentiation roadmap of murine placentation at single-cell resolution. *Cell Discov.* **9**, 30 (2023).
12. Woods, L., Perez-Garcia, V. & Hemberger, M. Regulation of placental development and its impact on fetal growth-new insights from mouse models. *Front. Endocrinol.* **9**, 570 (2018).
13. Simmons, D. G. et al. Early patterning of the chorion leads to the trilaminar trophoblast cell structure in the placental labyrinth. *Development* **135**, 2083–2091 (2008).
14. Yang, M. et al. Spatiotemporal insight into early pregnancy governed by immune-featured stromal cells. *Cell* **186**, 4271–4288 e4224 (2023).
15. Li, Q. et al. Base editing-mediated one-step inactivation of the Dnmt gene family reveals critical roles of DNA methylation during mouse gastrulation. *Nat. Commun.* **14**, 2922 (2023).
16. Meng, Y. et al. The role of DNA methylation in placental development and its implications for preeclampsia. *Front. Cell Dev. Biol.* **12**, 1494072 (2024).
17. Hemberger, M. Epigenetic landscape required for placental development. *Cell. Mol. Life Sci.* **64**, 2422–2436 (2007).
18. Tanaka, S., Nakanishi, M. O. & Shiota, K. DNA methylation and its role in the trophoblast cell lineage. *Int. J. Dev. Biol.* **58**, 231–238 (2014).
19. Andrews, S. et al. Mechanisms and function of de novo DNA methylation in placental development reveals an essential role for DNMT3B. *Nat. Commun.* **14**, 371 (2023).
20. Maekawa, R. et al. Genome-wide DNA methylation analysis revealed stable DNA methylation status during decidualization in human endometrial stromal cells. *BMC Genomics* **20**, 324 (2019).
21. Vaisvila, R. et al. Enzymatic methyl sequencing detects DNA methylation at single-base resolution from picograms of DNA. *Genome Res.* **31**, 1280–1289 (2021).
22. Zhang, Y. et al. Dynamic epigenomic landscapes during early lineage specification in mouse embryos. *Nat. Genet.* **50**, 96–105 (2018).
23. Luo, C. et al. Robust single-cell DNA methylome profiling with snmC-seq2. *Nat. Commun.* **9**, 3824 (2018).
24. Nichols, R. V. et al. High-throughput robust single-cell DNA methylation profiling with sciMETv2. *Nat. Commun.* **13**, 7627 (2022).
25. Uxa, S. et al. Ki-67 gene expression. *Cell Death Differ.* **28**, 3357–3370 (2021).
26. Pilia, G. et al. Mutations in GPC3, a glypican gene, cause the Simpson-Golabi-Behmel overgrowth syndrome. *Nat. Genet.* **12**, 241–247 (1996).
27. Wei, J. et al. Decreased Filamin b expression regulates trophoblastic cells invasion through ERK/MMP-9 pathway in pre-eclampsia. *Ginekol. Pol.* **90**, 39–45 (2019).
28. Zhang, Y., Yan, L., Liu, J., Cui, S. & Qiu, J. cGMP-dependent protein kinase II determines β-catenin accumulation that is essential for uterine decidualization in mice. *Am. J. Physiol. Cell Physiol.* **317**, C1115–C1127 (2019).
29. Elmore, S. A. et al. Histology atlas of the developing mouse placenta. *Toxicol. Pathol.* **50**, 60–117 (2022).

30. Akwii, R. G., Sajib, M. S., Zahra, F. T. & Mikelis, C. M. Role of angiopoietin-2 in vascular physiology and pathophysiology. *Cells* https://doi.org/10.3390/cells8050471 (2019).
31. Balsevich, G. et al. Stress-responsive FKBP51 regulates AKT2-AS160 signaling and metabolic function. *Nat. Commun.* **8**, 1725 (2017).
32. Downs, K. M. Systematic localization of Oct-3/4 to the gastrulating mouse conceptus suggests manifold roles in mammalian development. *Dev. Dyn.* **237**, 464–475 (2008).
33. Tan, B. F. et al. Decoding primitive endoderm - epiblast interactions using mouse ICM embryoids. Preprint at *bioRxiv* https://doi.org/10.1101/2024.12.28.630545 (2024).
34. Ross, C. & Boroviak, T. E. Origin and function of the yolk sac in primate embryogenesis. *Nat. Commun.* **11**, 3760 (2020).
35. Imaz-Rosshandler, I. et al. Tracking early mammalian organogenesis - prediction and validation of differentiation trajectories at whole organism scale. *Development* https://doi.org/10.1242/dev.201867 (2024).
36. Moore, J. E. et al. Expanded encyclopaedias of DNA elements in the human and mouse genomes. *Nature* **583**, 699–710 (2020).
37. Houle, M., Sylvestre, J. R. & Lohnes, D. Retinoic acid regulates a subset of Cdx1 function in vivo. *Development* **130**, 6555–6567 (2003).
38. Ang, S. L., Conlon, R. A., Jin, O. & Rossant, J. Positive and negative signals from mesoderm regulate the expression of mouse Otx2 in ectoderm explants. *Development* **120**, 2979–2989 (1994).
39. Krugmann, S. et al. Identification of ARAP3, a novel PI3K effector regulating both Arf and Rho GTPases, by selective capture on phosphoinositide affinity matrices. *Mol Cell* **9**, 95–108 (2002).
40. Varlet, I., Collignon, J. & Robertson, E. J. nodal expression in the primitive endoderm is required for specification of the anterior axis during mouse gastrulation. *Development* **124**, 1033–1044 (1997).
41. Lyons, A. et al. Insulin-like growth factor 1 signaling is essential for mitochondrial biogenesis and mitophagy in cancer cells. *J. Biol. Chem.* **292**, 16983–16998 (2017).
42. Yi, C., Kitamura, Y., Maezawa, S., Namekawa, S. H. & Cairns, B. R. ZBTB16/PLZF regulates juvenile spermatogonial stem cell development through an extensive transcription factor poising network. *Nat. Struct. Mol. Biol.* **32**, 1213–1226 (2025).
43. Zhang, S. et al. The role of SLC12A family of cation-chloride cotransporters and drug discovery methodologies. *J. Pharm. Anal.* **13**, 1471–1495 (2023).
44. He, Y. et al. Prosaposin maintains lipid homeostasis in dopamine neurons and counteracts experimental parkinsonism in rodents. *Nat. Commun.* **14**, 5804 (2023).
45. Yoo, H. C., Yu, Y. C., Sung, Y. & Han, J. M. Glutamine reliance in cell metabolism. *Exp. Mol. Med.* **52**, 1496–1516 (2020).
46. Hotamisligil, G. S. & Bernlohr, D. A. Metabolic functions of FABPs–mechanisms and therapeutic implications. *Nat. Rev. Endocrinol.* **11**, 592–605 (2015).
47. Maltepe, E., Bakardjiev, A. I. & Fisher, S. J. The placenta: transcriptional, epigenetic, and physiological integration during development. *J. Clin. Invest.* **120**, 1016–1025 (2010).
48. Ming, X. et al. Kinetics and mechanisms of mitotic inheritance of DNA methylation and their roles in aging-associated methylome deterioration. *Cell Res.* **30**, 980–996 (2020).
49. Charlton, J. et al. Global delay in nascent strand DNA methylation. *Nat. Struct. Mol. Biol.* **25**, 327–332 (2018).
50. Stewart-Morgan, K. R. et al. Quantifying propagation of DNA methylation and hydroxymethylation with iDEMS. *Nat. Cell Biol.* **25**, 183–193 (2023).

Methods

Animals

This study was approved by the Ethics Committee of the Institute of Biophysics, Chinese Academy of Sciences. The experimental procedures and animal care in this study were carried out in accordance with the guidelines set by the Institutional Animal Care and Use Committee of the Institutional Committee on Biosafety & Experimental Animal Management at the Institute of Biophysics, Chinese Academy of Sciences. The 6-week-old C57BL/6N mice used in this study were purchased from Beijing Vital River Laboratory Animal Technology Co. All animals were kept in a controlled environment with a 12-h light–dark cycle.

Sample collection and preparation

For the collection of embryos and uterine decidual samples, pregnant mice carrying embryos at the E5.5, E6.5, E7.5 and E8.5 stage were killed via cervical dislocation. The uterus was collected and rinsed with ice-cold PBS solution to remove any blood. Under a microscope, the uterine endometrium was gently separated to extract the embryos, which were still wrapped in uterine decidua. The embryos were washed once more with ice-cold PBS to ensure cleanliness. They were then centered in embedding molds, and any surface fluids were removed with a pipette. Pre-cooled Tissue-Tek O.C.T. Compound (Sakura, 4583) was added over the embryos and small bubbles were eliminated using a pipette. The molds were placed on dry ice for freezing, and the processed samples were stored at −80 °C for future experiments. The frozen sample block was then sectioned into 7-µm-thick slices for spatial library preparation.

Adaptors, barcodes and other key reagents

The oligonucleotides used for SmC-seq are detailed in Supplementary Table 4 and those employed for spatial RNA sequencing (modified DBiT-seq[51]) are listed in Supplementary Table 5.

Sample fixation, permeabilization and histone removal. For the preparation of SmC-seq libraries, frozen tissue sections were first thawed at room temperature for 10 min. Next, 0.2% formaldehyde was applied to the section, and the tissue was left to react at room temperature for 10 min. The slide was then immersed in DEPC-treated water for 3 min, after which it was removed and gently blow-dried with nitrogen gas.

A mono-hole polydimethylsiloxane (PDMS) chip (Suzhou Cchip Scientific Instrument) was positioned at the center of the slide and secured with clamps. To permeabilize the tissue, 80 µl of a homemade permeabilization buffer (10 mM Tris-HCl, pH 7.4, 10 mM NaCl, 3 mM $MgCl_2$ and 0.5% Triton-X-100) was added into the hole in the chip, and the tissue was incubated at room temperature for 35 min. After incubation, the tissue section was washed twice with DEPC-treated water. Next, 90 µl of 0.2 N HCl was applied to the tissue section in three separate aliquots, with each addition incubated at room temperature for 15 min to facilitate the removal of histones from the chromatin. After the reaction, the tissue section was washed twice with DPBS to finalize the preparation.

Labeling of spatial information on DNA fragments. To integrate adaptors into the DNA fragment flanking regions, universal adaptors A and B were first loaded onto Tn5 transposase (Novoprotein) according to the manufacturer's instructions. The adaptors were pre-mixed in equal proportions. Then, 30 µl of the tagmentation mixture, comprising 1× homemade Tagmentation Buffer (33 mM Tris-Ac, 66 mM KAc, 10 mM $MgAc_2$, 16% *N*,*N*-dimethylformamide and 0.02% digitonin) and 2 µl of the Tn5 transposase mixture was applied to the tissue sample to fragment the genomic DNA and insert the adaptors. The reaction was conducted at 37 °C for 45 min. To ensure efficient adaptor insertion, this process was repeated twice.

The mono-hole PDMS chip was substituted with a PDMS microfluidic chip containing 96 channels, each with a diameter of either 10 µm or 20 µm (Suzhou Cchip Scientific Instrument). To facilitate the ligation of the first-round barcodes to the DNA fragments, 4 µl of barcode mixture A (comprising 1× T4 Ligase Buffer (NEB), 15 U μl^{-1} T4 DNA Ligase (NEB), 0.1% Triton-X-100 and 11 µM barcode A) was introduced into each channel. The mixture was then aspirated through the channels under a vacuum. The sample was subsequently incubated at 37 °C for 1 h. Following incubation, the reaction in each channel was quenched by adding 4 µl of barcode blocking mixture A (containing 4.4 µM Blocking A and 1× T4 Ligase Buffer), followed by a 20-min incubation at 37 °C. The microfluidic chip was then carefully removed, and the slide was thoroughly washed with DEPC-treated water to complete the process.

To perform the ligation of the second round of barcodes, the slide was fitted with an additional PDMS microfluidic chip, oriented perpendicular to the previous one. Then, 4 µl of barcode mixture B, consisting of 1× T4 Ligase Buffer, 15 U μl^{-1} T4 DNA Ligase, 0.1% Triton-X-100 and 11 µM barcode B, was introduced into each channel. This mixture was then drawn through the channels under vacuum. The sample was incubated at 37 °C for 1 h to allow ligation. Following the incubation, the ligation reaction was quenched by adding 4 µl of barcode blocking mixture B, which contained 4.4 µM Blocking B and 1× T4 Ligase Buffer, and the reaction was further incubated at 37 °C for an additional 20 min. After the removal of microfluidic chip, the slide was thoroughly washed with DEPC-treated water to complete the process.

After completing two rounds of barcoding, a clean mono-hole PDMS chip was positioned at the center of the slide and fixed with clamps. 50 µl of homemade DNA lysis buffer (comprising 10 mM Tris-HCl (pH 8), 5 mM EDTA, 150 mM NaCl, 0.5% SDS and 4 mg ml^{-1} proteinase K) was added to the sample. The sample was then incubated at 55 °C for 1 h to facilitate efficient cell lysis. Following incubation, the supernatant was aspirated by pipetting ten times and transferred to a 1.5-ml Eppendorf tube. The microfluidic hole was then rinsed twice with lysis buffer, and the collected supernatant was added to the same tube. The tube was subsequently placed in a 55 °C dry bath incubator overnight to ensure complete digestion and DNA release. The DNA was then purified using SPRIselect beads (Beckman Coulter), and the final DNA was eluted with nuclease-free water for downstream applications.

Preparation of spike-in controls. A CpG-methylated lambda phage spike-in DNA was generated by methylating the CpG sites of unmethylated lambda DNA (NEB) using CpG Methyltransferase M.SssI (NEB), following the manufacturer's protocol. Additionally, a 5-hydroxymethylated pSP64 plasmid DNA fragment was synthesized by Takara and utilized as a 5hmC spike-in control. The CpG-methylated lambda spike-in DNA and the 5-hydroxymethylated pSP64 spike-in DNA were combined in equal ratios. The resulting spike-in DNA mixture was then tagmented using Tn5 transposase, followed by barcode ligation as previously described. The final product was stored at −20 °C until further use.

Cytosine conversion. The eluted DNA was subjected to an extension reaction using Bst DNA polymerase (NEB) to replace unmodified cytosines in the adaptors and barcodes with 5-hydroxymethylated cytosines (5hmCs). The extension reaction mixture, consisting of 1× ThermoPol Buffer (NEB), 6 mM $MgSO_4$, 0.2 mM dATP, 0.2 mM dTTP, 0.2 mM 5-hydroxymethyl-dCTP (Abcam), 0.2 mM dGTP, 320 U ml^{-1} Bst DNA polymerase (NEB, M0275S), 0.05 ng of the spike-in DNA mix and the eluted DNA, was incubated in a 65 °C dry bath for 45 min. Following the reaction, the extended DNA was purified using 1.4× SPRIselect beads and eluted in nuclease-free (NF) water.

To distinguish the 5mCs in the extended DNA fragments from other cytosines, the 5mCs were oxidized by TET2, and the resulting 5hmCs or 5caC, along with the 5hmCs incorporated into the adaptors and barcodes during the extension step, were glucosylated in a one-step

reaction using T4 Phage β-glucosyltransferase (NEB), following the manufacturer's instructions. The reaction mixture was incubated at 37 °C in a dry bath for 2 h. Following glucosylation, the DNA was purified using 1.4× SPRIselect beads and eluted in NF water.

For DNA denaturation, 4 µl of 0.1 M NaOH was mixed with 16 µl of the eluted DNA and incubated in a pre-heated 50 °C thermal cycler for 10 min, with the heated lid set to 65 °C. The sample was then immediately transferred to ice. The denatured DNA was deaminated using apolipoprotein B mRNA-editing catalytic polypeptide (APOBEC) from the NEBNext Enzymatic Methyl-seq Conversion Module (NEB, E7125S). The reaction mixture was incubated overnight at 37 °C in a thermal cycler with the heated lid set to 50 °C. Finally, the DNA was purified using 1.4× SPRIselect beads and eluted in NF water.

PCR amplification and sequencing. To set up the PCR, 25 µl of KAPA HiFi HotStart Uracil+ ReadyMix (2×) (KAPA), 1 µl of DNA primer A (10 µM) and 1 µl of DNA primer B (10 µM) were mixed with 23 µl of deaminated DNA and thoroughly combined. The PCR program consisted of an initial denaturation step at 95 °C for 3 min, followed by ten cycles of 98 °C for 20 s, 58 °C for 15 s and 72 °C for 60 s, and a final extension step at 72 °C for 5 min. The resulting libraries were sequenced on the Illumina NovaSeq 6000 platform using paired-end 150 bp sequencing.

Spatial transcriptome library preparation

Sample fixation and permeabilization. To prepare spatial transcriptome libraries, a modified version of the DBiT-seq protocol was employed. First, the frozen slide was allowed to thaw at room temperature for 10 min. The tissue was then fixed using 4% formaldehyde at room temperature for 20 min. After fixation, the slide was rinsed thoroughly with DEPC-treated water and dried using a blow-dryer. Next, the slide, a single-hole PDMS chip, and clamps were assembled following the previously described method. A 50-µl RNA permeabilization mixture, containing 0.5% Triton-X-100, 0.1 U µl^{-1} RNase Inhibitor (Enzymatics) and 0.05 U µl^{-1} SUPERase In RNase Inhibitor (Invitrogen), was applied to the tissue and incubated at room temperature for 45 min. Finally, the tissue was washed twice with 50 µl ice-cold PBS.

Reverse transcription (first-strand synthesis). To perform first-strand complementary DNA synthesis, 48 µl of reverse transcription mixture was prepared, containing 12.45% PEG6000, 1× RT buffer, 25 U µl^{-1} Maxima H Minus Reverse Transcriptase (Thermo Scientific), 10 µM RT primer, 0.5 mM dNTP mix (NEB) and 0.4 U µl^{-1} RNase inhibitor (Enzymatics). This mixture was combined with 12 µl of the RNA permeabilization mixture and applied to the tissue. The slide was incubated at room temperature for 30 min, followed by incubation at 42 °C for 90 min. After incubation, the slide was thoroughly washed with DEPC-treated water and blow-dried.

Insertion of spatial information into RNA. To incorporate spatial barcodes into the RNA, a PDMS microfluidic chip was assembled onto the slide as previously described. For each channel, 3 µl of RNA barcode buffer (1.8× T4 Ligase buffer, 30 U µl^{-1} T4 DNA Ligase, 0.75× NEB Buffer 3.1, 0.2% Triton-X-100, 5 U µl^{-1} RNase Inhibitor (Enzymatics) and 0.1 U µl^{-1} SUPERase•In RNase Inhibitor) and 1 µl of RNA barcode A were added. The slide was incubated at 37 °C for 1 h. Subsequently, 4 µl of barcode blocking mixture A was added to each channel and incubated at 37 °C for 20 min. The slide was then washed thoroughly by soaking in DEPC-treated water and blow-dried.

A second microfluidic chip, with channels oriented perpendicular to the first, was attached to the slide. For each channel, 3 µl of RNA barcode buffer and 1 µl of RNA barcode B were added, followed by incubation at 37 °C for 1 h. Next, 4 µl of barcode blocking mixture B was added to each channel and incubated at 37 °C for 20 min. The slide was again washed thoroughly with DEPC-treated water and blow-dried.

cDNA purification. A clean single-hole PDMS chip was placed onto the slide and secured with a clamp. A 50-µl aliquot of homemade RNA lysis buffer (10 mM Tris-HCl, pH 8.0, 50 mM EDTA, 200 mM NaCl, 2.5% SDS and 4 mg ml^{-1} proteinase K) was added to the sample. The slide was incubated at 55 °C for 2 h. After incubation, the supernatant was pipetted ten times to mix and transferred to a 1.5-ml tube. The hole was washed twice with lysis buffer, and the supernatant was also transferred to the same tube. The tube was stored at −80 °C until further use.

For each sample, 40 µl of Dynabeads MyOne Streptavidin C1 beads (Thermo Fisher, 65001) were washed three times with 1× B&W buffer (5 mM Tris-HCl, pH 8.0, 0.5 mM EDTA and 1 M NaCl) supplemented with 0.05% Tween-20. The beads were then resuspended in 100 µl of 2× B&W buffer supplemented with 2 µl SUPERase•In RNase Inhibitor. The extracted cDNA from the stored tube was purified using the DNA Clean & Concentrator kit (Zymo, D4003) and eluted in 100 µl of NF water.

Reverse transcription (second-strand synthesis). The purified 100 µl DNA solution was thoroughly mixed and incubated with an equivalent volume of resuspended Dynabeads MyOne Streptavidin C1 beads at room temperature for 1 h. The beads were then washed twice with 1× B&W buffer supplemented with 0.05% Tween-20, followed by a single wash with STE buffer (10 mM Tris, pH 8.0, 1 mM EDTA and 50 mM NaCl). The beads were resuspended in a template switch mixture containing 14% PEG6000, 1× Maxima RT buffer, 4% Ficoll PM-400, 1 mM dNTP, 2.5 µM TSO, 10 U µl^{-1} Maxima Reverse Transcriptase and 1 U µl^{-1} RNase Inhibitor (Enzymatics). The mixture was incubated at room temperature for 30 min, followed by incubation at 42 °C for 90 min. After incubation, the beads were sequentially rinsed with STE buffer and NF water.

The beads were then resuspended in PCR mixture A, consisting of 1× KAPA HiFi PCR mix (KAPA), 400 nM RNA primer A, and 400 nM RNA primer B. The cDNA was amplified using the following program: initial denaturation at 95 °C for 3 min, followed by six cycles of 98 °C for 30 s, 65 °C for 45 s and a final extension at 72 °C for 3 min. The supernatant was purified using 0.8× SPRIselect beads and eluted in NF water. The DNA concentration was quantified using a Qubit 4 fluorometer (Thermo Fisher).

cDNA tagmentation. The RNA Tn5 mixture was prepared by loading annealed RNA Tn5 adaptor1 and RNA Tn5 adaptor2 oligonucleotides onto Trueprep Tn5 (Vazyme) according to the manufacturer's instructions. The tagmentation mixture, containing 1× tagment buffer L (Vazyme), 2 µl of RNA Tn5 mixture (per 50 ng cDNA), and the sample cDNA, was incubated at 55 °C for 10 min. After tagmentation, the fragmented cDNA was purified using 0.9× SPRIselect beads and eluted in NF water.

PCR amplification and sequencing. The PCR mixture B, comprising 1× NEBNext Ultra II Q5 Master Mix (NEB), 1.25 µM RNA primer C, 1.25 µM RNA primer D and the sample cDNA, was subjected to the following program: initial incubation at 72 °C for 5 min, denaturation at 95 °C for 3 min, followed by four cycles of 98 °C for 20 s, 65 °C for 15 s and 72 °C for 1 min, with a final extension at 72 °C for 2 min. The reaction product was purified using 0.7× SPRIselect beads and eluted in NF water. The final libraries were sequenced on the Illumina NovaSeq 6000 platform using paired-end 150 bp sequencing.

Immunostaining

The immunostaining assays were carried out as described[52]. In brief, the 7-µm cryosections were placed at room temperature for 10 min to equilibrate. The sections were fixed with 100 µl of 2% paraformaldehyde at room temperature for 50 min. After two washes with 100 µl of PBS (5 min each), the sections were permeabilized with 100 µl of 0.5% Triton-X-100 in PBS for 40 min, followed by two rounds of rinsing with PBS (10 min each). The slides were immersed in a Schieferdecker jar filled with 0.01 M sodium citrate pH 6.0, then placed into a

microwaveable dish containing pre-boiled water. The jar containing the slides was transferred to a microwave oven and heated at full power for 6 min. After heating, the jar was removed and allowed to cool to room temperature for 10 min. The slides were then rinsed in PBS in a rocking jar for 15 min. Subsequently, the sections were blocked with 100 µl of blocking solution (2% BSA, 1% goat serum and 1% donkey serum in PBS) at room temperature for 1 h. Primary antibodies diluted in the blocking solution (100 µl) were applied and incubated at room temperature for 2 h. We used 5-methylcytosine antibody (Abcam, #ab10805, 1:100), Mki67 antibody (Proteintech, 28074-1-AP, 1:200 dilution), Psap antibody (Proteintech, 10801-1-AP), Vimentin antibody (Proteintech, 10366-1-AP, 1:200), Alexa Fluor 647 anti-mouse CD31 antibody (BioLegend, 102415, 1:200 dilution) and Alexa Fluor 647 anti-cytokeratin (pan reactive) antibody (BioLegend, 628604, 1:200 dilution) in this study. After removal of the antibody solution, the slides were washed three times with 200 µl of PBST (0.2% Tween-20 in PBS, 15 min for each wash). Secondary antibodies diluted 1:250 in blocking solution (100 µl) were applied and incubated at room temperature for 1 h. The secondary antibodies used in these assays included donkey anti-mouse IgG (H + L) highly cross-adsorbed secondary antibody, Alexa Fluo 488 (Invitrogen, A-21202), donkey anti-rabbit IgG (H + L) highly cross-adsorbed secondary antibody and Alexa Fluor 555 (Invitrogen, A-31572). After removal of the antibody solution, the slides were washed once with 200 µl of PBST (15 min). Then, 100 µl of Hoechst 33342 solution (Invitrogen, H3570, 50 µg ml^{-1}) was applied and incubated at room temperature for 10 min. After three washes with 200 µl of PBST (15 min for each wash), the sections were mounted with cover slips using ProLong Gold Antifade Mountant (Thermo Fisher, P36930). The images were captured using an Olympus Fluoview FV3000 confocal laser scanning microscope. Fluorescent intensities were analyzed by ImageJ software[53].

Diffusion distance evaluation

Barcodes A DNA conjugated with fluorescent dyes was used to evaluate the diffusion distance of DNA using fluorescence microscopy. Two types of barcode A, labeled with cyanine3 (Cy3) or 6-carboxyfluorescein (6-FAM), were used. For barcode A ligation, cells in adjacent microchannels were ligated with distinct dyes to evaluate channel leakage. The E5.5 mouse embryo frozen slide was subjected to three rounds of HCl treatment, followed by Tn5-mediated adaptor ligation as described in SmC-seq procedure. A microfluidic chip featuring 10-µm-wide microchannels with 5-µm-wide intervals between them was used. Then, 2 µM barcodes A labeled fluorescently was ligated to the end of the Tn5 adaptor at 37 °C for 1 h. After ligation, the microchannels were washed once using barcode blocking mixture A, and then observed under a fluorescence microscope (Olympus CKX53). As described previously[51], the diffusion distance is defined as the distance from the edge of microchannel to where the fluorescence signal decreased to half of its peak intensity within the microchannel. This was analyzed using ImageJ software.

Spatial transcriptome data analysis

Quality control, alignment and normalization. During the initial processing of raw transcriptomic data, unique molecular identifiers (UMIs), RNA barcode 1 and RNA barcode 2 were extracted from the Read 2 FASTQ files. Subsequently, the Read 1 FASTQ files were aligned to the mouse reference genome (GRCm38) using STpipeline (v.1.7.238)[54]. The aligned reads were annotated according to Gencode release M11 to generate a GE matrix. In this matrix, the row labels correspond to spatial coordinates derived from the combined information of RNA barcode 1 and RNA barcode 2, while the column labels represent individual genes. Next, the GE matrices for each sample were processed using Seurat (v.4.1.1)[55]. Initially, quality control was conducted to filter out low-quality pixels, retaining only those with UMI counts exceeding 300 for downstream analysis. Following this, the SCTransform method was employed to independently normalize each sample. This normalization utilized a regularized negative binomial regression model, with the parameter variable.features.*n* = 3,000 set to identify and retain the top 3,000 highly variable genes for subsequent analysis.

Integrative analysis of multiple datasets. To integrate our spatial transcriptomic datasets with published single-cell and spatial transcriptomic datasets, we employed Seurat's built-in integration pipeline. Briefly, the SelectIntegrationFeatures function was first used to identify a set of integration features from the selected clusters, with the parameter nfeatures = 1,500 to ensure a robust and representative feature set. The PrepSCTIntegration function was then applied to prepare the data for integration, with the anchor.features parameter set to the output of SelectIntegrationFeatures. Next, the FindIntegrationAnchors function was utilized to identify integration anchors, using the parameters normalization.method = 'SCT' and retaining the previously defined anchor.features. Finally, data integration performed using the IntegrateData function, with the parameters normalization.method = 'SCT' and k.weight = 50.

Clustering analysis and annotation. Upon completion of the integration process, the integrated dataset was designated as the default assay using the command DefaultAssay set to 'integrated'. Principal-component analysis (PCA) was subsequently performed, with the parameter npcs = 30. This was followed by UMAP dimensionality reduction, configured with the parameters reduction = 'pca' and dims = 1:30 to project the data into a lower-dimensional space for visualization and interpretation. Neighboring cells were identified using the same PCA-based reduction (reduction = 'pca' and dims = 1:30). Finally, clustering analysis was conducted, with the resolution parameter dynamically adjusted to reflect the specific biological context and dataset characteristics.

GO enrichment analysis. The clusterProfiler package[56] and associated databases were loaded to perform GO enrichment analysis. Gene lists were prepared and converted into Entrez gene IDs to facilitate downstream analysis. The enrichGO function was then applied to conduct GO enrichment analysis, with the following parameters: ont = 'ALL' to include all GO categories (biological process, molecular function, and cellular component), pAdjustMethod = 'BH' to correct for multiple testing using the Benjamini–Hochberg method, and pvalueCutoff = 0.01 and qvalueCutoff = 0.05 to filter for statistically significant GO terms. Finally, the enrichment results were visualized using the ggplot2 package, generating bar plots and bubble plots to effectively display the significantly enriched GO terms.

Cell differentiation trajectory analysis. To elucidate the dynamic changes and developmental processes underlying cell lineages, two complementary methods were employed for inferring cell differentiation trajectories: RNA velocity-based inference and pseudotime analysis.

RNA velocity analysis was performed using scVelo (v.0.2.4)[57], leveraging RNA splicing information to infer developmental trajectories. The abundances of spliced and unspliced mRNAs were quantified using Velocyto (v.0.17.17)[58] with default parameters. A *k*-nearest neighbor graph ($k = 8$) was constructed, with redundant meta-cells ($n > 5$) removed to streamline the analysis. The count matrix was then filtered and normalized using the scv.pp.filter_and_normalize function in scVelo. RNA synthesis and degradation rates were estimated using a kinetic model implemented in the scv.tl.recover_dynamics function, and velocity vectors were computed based on cosine similarity between meta-cells, capturing the direction and magnitude of transcriptional changes. Finally, UMAP embeddings derived from Seurat analysis were integrated with RNA velocity data, and the scv.pl.velocity_embedding_stream function was used to visualize RNA velocities as streamlines.

SmC-seq data analysis

The analysis of spatial methylation data involves several key steps, which have been integrated into an analysis pipeline. The integrated pipeline can directly process raw FASTQ files and generate outputs containing both spatial information and DNA methylation profile for the corresponding tissue section.

Quality control. To ensure the quality of sequencing data from the methylation library, a quality control step was implemented, in which reads with unmatched barcode combinations were removed using UMI-tools (v.1.1.2)[59]. Crick and Watson strand identities were then determined based on specific bases located between two rounds of barcodes and processed separately in the subsequent analysis. Finally, adaptor removal and low-quality read filtering were carried out using Trim Galore (v.0.6.6).

Sequence read alignment. For spatial DNA methylation raw data, DNA barcode A and B sequences were extracted from read 2 of the FASTQ file. Filtered reads were then mapped to the mouse genome (GRCm39)[60], followed by an iterative mapping step to improve the mapping rate. This step included trimming unmapped reads by 5 bp at their 5′ end and re-mapping them to the mouse genome, which was repeated five times. Subsequently, the resulting files from the iterative mapping process were merged to obtain the final optimal result. The BAM file was then divided into multiple subsets based on the unique combinations of two rounds of barcodes, with each subset containing only a single barcode combination representing a distinct pixel.

Deduplication and ML calculation. The BAM file subsets were subjected to deduplication using the deduplicate_bismark function in Bismark (v.0.23.0). Subsequently, the DNA methylation profile for each subset was extracted using methylation_extractor function in Bismark. The spatial distribution of MLs was then calculated and visualized using ComplexHeatmap (v.2.14.0)[61].

Pixel alignment. The integration of DNA methylation and RNA spatial data was achieved through the spatial alignment of their respective images using an affine transformation. Initially, both the SmC-seq methylation data and DBiT-seq RNA images were preprocessed by converting them to grayscale and downsampling to 192 × 192 pixels, preserving spatial structure while reducing resolution[62]. Binary edge detection was applied to highlight tissue boundaries, aiding in alignment. Affine image registration was performed using the SimpleITK package[63], with the RNA image as the fixed image and the methylation image as the moving image. The registration process involved manual tuning steps, including grayscale threshold adjustment, Gaussian smoothing and affine transformation optimization, which were iterated for the best alignment. The quality of the alignment was assessed using the Dice coefficient, ensuring a strong spatial overlap (Dice coefficient > 0.85) between the methylation and RNA dot-plots. The resulting affine transformation matrix was applied to the methylation data to map it onto the RNA spatial framework. Finally, a filtering step was implemented to exclude spatially unreliable methylation points (those shifting more than 10 µm from the nearest RNA pixel), ensuring only the most accurate data were retained for joint analysis of RNA expression and DNA methylation patterns.

Co-clustering analysis. To validate the quality of the spatial methylation library, we conducted unsupervised co-clustering of our SmC-seq data with previously published single-cell methylation data from mouse embryos[9]. DNA MLs of all gene body regions after quality control were used as features for co-clustering analysis. The average DNA ML of CpGs in a pixel was calculated by the formula: average DNA ML = number of CpGs with methylation/(number of CpGs with methylation + number of CpGs without methylation). These regions were filtered based on the criterion that more than five CpGs were covered in over 20% of all pixels. A DNA methylation matrix was generated, with columns representing features and rows representing individual pixels in SmC-seq data or cells in the published single-cell-5mC data. Empty values in the matrix were replaced with the average of non-empty values in the same column. Our data also show that DNA MLs of gene body or promoter regions are usually 0 and 1. Because the average ML is close to 0.5 and the probability of 0.5 is relatively low, we filled the missing values with 0.5 for one column with excessive missing values, which will have limited effects on the features of the matrix. The top 20 principal components (PCs) for each pixel or cell were computed using the prcomp function in the R package stats (v.4.2.3). Finally, after dimension reduction via UMAP, the results were visualized in two dimensions using the R package umap (v.0.2.10.0).

Clustering analysis of spatial DNA methylation data. To simultaneously incorporate spatial locations and MLs in clustering analysis, we implemented a new clustering method, which integrated the Euclidean distance matrix with the ML matrix. We first generated a Euclidean distance matrix for all pixels (for example, for a slice with 96 × 96 pixels, a matrix with 9,216 rows and 9,216 columns). Then we identified the critical anchors with important spatial information by using the FindIntegrationAnchors function in Seurat (v.4.1.1). Next, the weight of the dimensionally reduced spatial matrix and the ML matrix is the same in the downstream analysis. This was followed by PCA and clustering using the *k*-means algorithm from the R package stats (v.4.2.3). We also combined k-means with the get_clust_tendency and clusGap functions in the R package factoextra (v.1.0.7) to identify the optimal cluster number. Finally, the selected PCs were dimensionally reduced into a two-dimensional object using the UMAP algorithm in the R package umap. The in situ spatial distribution of all these clusters was visualized.

DMR analysis and functional enrichment analysis. To perform DMR analysis, the genome was divided into 300-bp bins, which were filtered to include only those containing more than five CpGs covered by sequencing data. Significance was assessed using Fisher's extract test in the R package stats (v.4.2.3). DMRs were selected based on a *P* value threshold <0.01. To control the false discovery rate (FDR) in multiple hypothesis testing of DMRs, we performed the Benjamini–Hochberg (BH) method with a cutoff FDR level of 0.1. We identified DMR-associated promoters, defining the promoter region as 2 kb upstream and 500 bp downstream of the transcription start site for each gene. We also identified DMR-associated genes, defined as the gene closest to the DMR. GO term enrichment analyses for both DMR-associated promoters and genes were conducted through a series of R packages, including clusterProfiler (v.4.6.2)[56], enrichplot (v.1.18.4), org.Mm.eg.db (v.3.16.0) and biomaRt (v.2.54.1)[64].

Statistical analysis

Statistical analysis was performed using R (v.4.2.3). The statistical tests used in this study are specified in figure legends or bioinformatics analysis sections.

Reporting summary

Further information on research design is available in the Nature Portfolio Reporting Summary linked to this article.

Data availability

The raw sequence data of SmC-seq and spatial RNA-seq reported in this study have been deposited in the Genome Sequence Archive in National Genomics Data Center China National Center for Bioinformation (accession numbers CRA023723 and CRA028148).

Code availability

The code used in this study is deposited in GitHub (https://github.com/LiuLab888/spatial-5mC-project/).

References

51. Liu, Y. et al. High-spatial-resolution multi-omics sequencing via deterministic barcoding in tissue. *Cell* **183**, 1665–1681.e18 (2020).
52. Beaujean, N., Salvaing, J., Hadi, N. A. A. & Pennings, S. Antibody-based detection of global nuclear DNA methylation in cells, tissue sections, and mammalian embryos. *Methods Mol. Biol.* **1708**, 59–80 (2018).
53. Collins, T. J. ImageJ for microscopy. *Biotechniques* **43**, 25–30 (2007).
54. Navarro, J. F., Sjostrand, J., Salmen, F., Lundeberg, J. & Stahl, P. L. ST Pipeline: an automated pipeline for spatial mapping of unique transcripts. *Bioinformatics* **33**, 2591–2593 (2017).
55. Hao, Y. et al. Integrated analysis of multimodal single-cell data. *Cell* **184**, 3573–3587 e3529 (2021).
56. Wu, T. et al. clusterProfiler 4.0: a universal enrichment tool for interpreting omics data. *Innovation* **2**, 100141 (2021).
57. Bergen, V., Lange, M., Peidli, S., Wolf, F. A. & Theis, F. J. Generalizing RNA velocity to transient cell states through dynamical modeling. *Nat. Biotechnol.* **38**, 1408–1414 (2020).
58. La Manno, G. et al. RNA velocity of single cells. *Nature* **560**, 494–498 (2018).
59. Smith, T., Heger, A. & Sudbery, I. UMI-tools: modeling sequencing errors in unique molecular identifiers to improve quantification accuracy. *Genome Res.* **27**, 491–499 (2017).
60. Krueger, F. & Andrews, S. R. Bismark: a flexible aligner and methylation caller for bisulfite-seq applications. *Bioinformatics* **27**, 1571–1572 (2011).
61. Gu, Z., Eils, R. & Schlesner, M. Complex heatmaps reveal patterns and correlations in multidimensional genomic data. *Bioinformatics* **32**, 2847–2849 (2016).
62. van der Walt, S. et al. scikit-image: image processing in Python. *PeerJ* **2**, e453 (2014).
63. Lowekamp, B. C., Chen, D. T., Ibáñez, L. & Blezek, D. The design of simpleITK. *Front. Neuroinform.* **7**, 45 (2013).
64. Durinck, S., Spellman, P. T., Birney, E. & Huber, W. Mapping identifiers for the integration of genomic datasets with the R/Bioconductor package biomaRt. *Nat. Protoc.* **4**, 1184–1191 (2009).

Acknowledgements

This study was supported by the grants from National Key Research and Development Program of China (2024YFA1802100 to L.G.), Shenzhen Medical Research Fund (B2504001 to J.L.), Strategic Priority Research Program of the Chinese Academy of Sciences (XDB1000302 to J.L.), National Natural Science Foundation of China (32430024 to J.L. and 32471502 to L.G.), the Key-Area Research and Development Program of Guangdong Province (2023B1111020006 to J.L.) and 2023 International Science and Technology Cooperation Projects in Guangzhou Development District (2023GH09 to X.Y.). We thank S. Jia for assistance with reagent ordering and administrative support and Z. Xing for help with the animal experiments. We also thank D. Duo and Y. Teng for technical support with confocal imaging.

Author contributions

J.L. supervised the project; J.L. and L.G. conceptualized the project; X.S., L.G. and Y.T. designed and developed the method; X.S., J.H. and L.G. performed the experiments; Y.T., X.S., J.H. and L.G. performed the computational analysis; M.B. was responsible for data visualization and review of the paper; X.S., L.G., Y.T. and J.L. wrote the original draft; and X.Y. was responsible for funding acquisition and reviewing the paper. All authors contributed to revising the paper and approved the final version.

Competing interests

The authors declare that a patent application has been submitted.

Additional information

Extended data is available for this paper at https://doi.org/10.1038/s41592-026-03079-w.

Supplementary information The online version contains supplementary material available at https://doi.org/10.1038/s41592-026-03079-w.

Correspondence and requests for materials should be addressed to Lei Gao or Jiang Liu.

Peer review information *Nature Methods* thanks the anonymous reviewers for their contribution to the peer review of this work. Peer reviewer reports are available. Primary Handling Editor: Madhura Mukhopadhyay and Lei Tang, in collaboration with the *Nature Methods* team.

https://doi.org/10.1038/s41592-026-03079-w

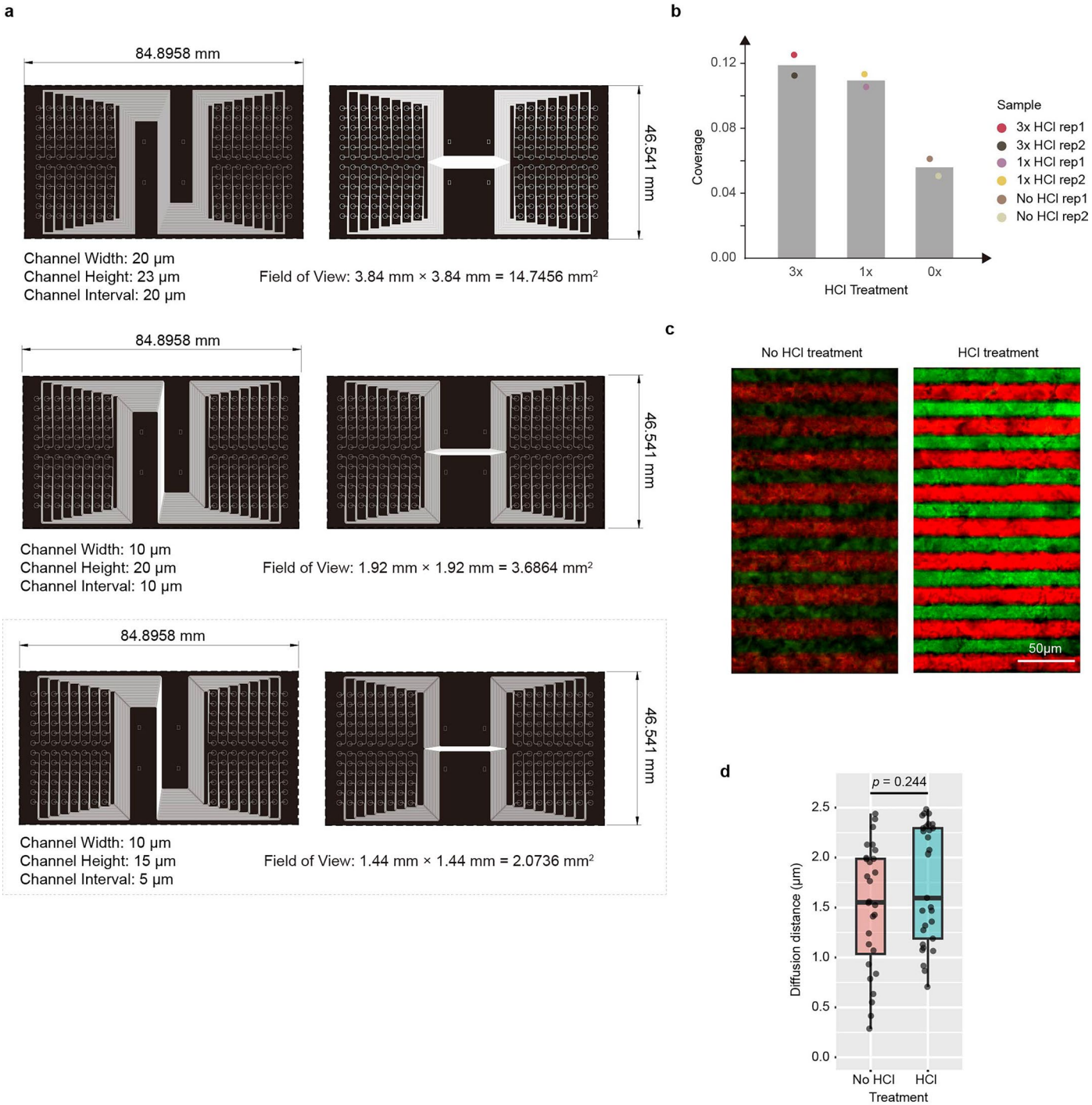

Extended Data Fig. 1 | Microchip design and effects of HCl treatment on DNA diffusion. a, Schematic designs of the three versions of microchannel chips used in this study. **b**, Genome coverage of SmC-seq at the pseudobulk level under three different HCl treatment conditions. "3× HCl" indicates treatment with 0.2 N HCl at room temperature for 5 min per round, repeated for three rounds; "1× HCl" indicates a single round of the same treatment; "No HCl" indicates no HCl treatment. "Rep" denotes replicate. For each of the six samples, 69,256,892 raw reads were used as input. Genome coverage was defined as the proportion of CpGs across the whole genome that were covered by sequencing reads. **c**, Fluorescent imaging measuring cross-channel diffusion distances and possible crosstalk between two neighboring channels by alternately flowing 5-Carboxyfluorescein (5-FAM, Green)-labeled Barcode A and Cyanines3 (Cy3, Red)-labeled Barcode A in adjacent channels. E5.5 embryonic tissue sections, with or without three rounds of HCl treatment, were evaluated and compared. The microchannel chip used here consists of 10-μm-width channels with 5 μm spacing. **d**, Quantification of diffusion distances with and without three rounds of HCl treatment. Each group includes 30 channels and 29 intervals. Boxes denote the interquartile range (25th–75th percentiles), with the median marked inside. Whiskers extend to the furthest observations within 1.5 × IQR from the quartiles. Two-side t-test was used for statistical analysis.

https://doi.org/10.1038/s41592-026-03079-w

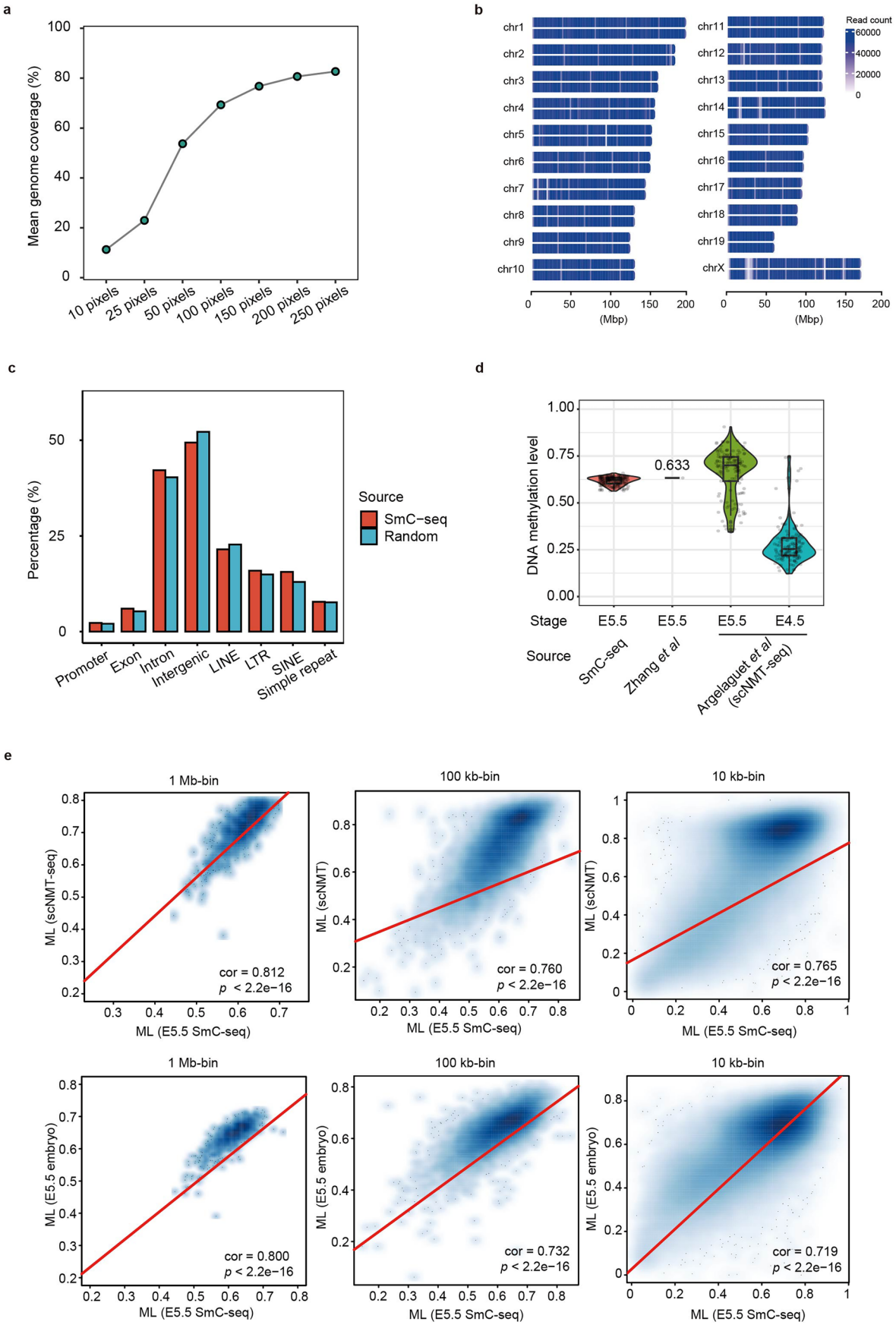

Extended Data Fig. 2 | See next page for caption.

https://doi.org/10.1038/s41592-026-03079-w

Extended Data Fig. 2 | Evaluation SmC-seq in E5.5 mouse embryo. a, Line chart showing CpG genome coverage based on pseudobulk data generated by merging different number of pixels (10 µm × 10 µm) in the SmC-seq data of the E5.5 embryo. **b**, Read distribution from the SmC-seq data of the E5.5 embryo across all chromosomes in the mouse. The number of reads in each non-overlapping 1-million-base-pair (Mbp) bin is shown. For each chromosome, the upper strand represents the Watson strand, while the bottom strand represents the Crick strand. **c**, Bar chart depicting the percentages of different genome elements covered by E5.5 mouse embryo sequencing data using SmC-seq (red) compared with a set of random genomic regions matched for sequencing read length and number (blue). **d**, DNA methylation levels of mouse E5.5 epiblast (embryo) measured by SmC-seq (n = 217 pixels) or from published data. The published data including bulk DNA methylation sequencing data and scNMT-seq data, were obtained from Zhang *et al.*, (2018) (n = 1 sample) and Argelaguet *et al.*, (2019) (E5.5, n = 134 cells; E4.5, n = 133 cells), respectively. The global DNA methylation level was calculated for each cell or sample. Boxes denote the interquartile range (25th–75th percentiles), with the median marked inside. Whiskers extend to the furthest observations within 1.5 × IQR from the quartiles. **e**, Scatter plots comparing DNA methylation levels in non-overlapping bins of various sizes (1 Mb, 100 kb, 10 kb) between E5.5 embryo measured by SmC-seq and E5.5 epiblast cells measured by scNMT-seq (upper) or bulk DNA methylation sequencing (bottom). Pearson's correlation coefficients were shown (cor). Linear regression lines are included. P value < 2.2e-16 indicates that the p value is smaller than the smallest positive floating-point number that can be represented by the computer.

https://doi.org/10.1038/s41592-026-03079-w

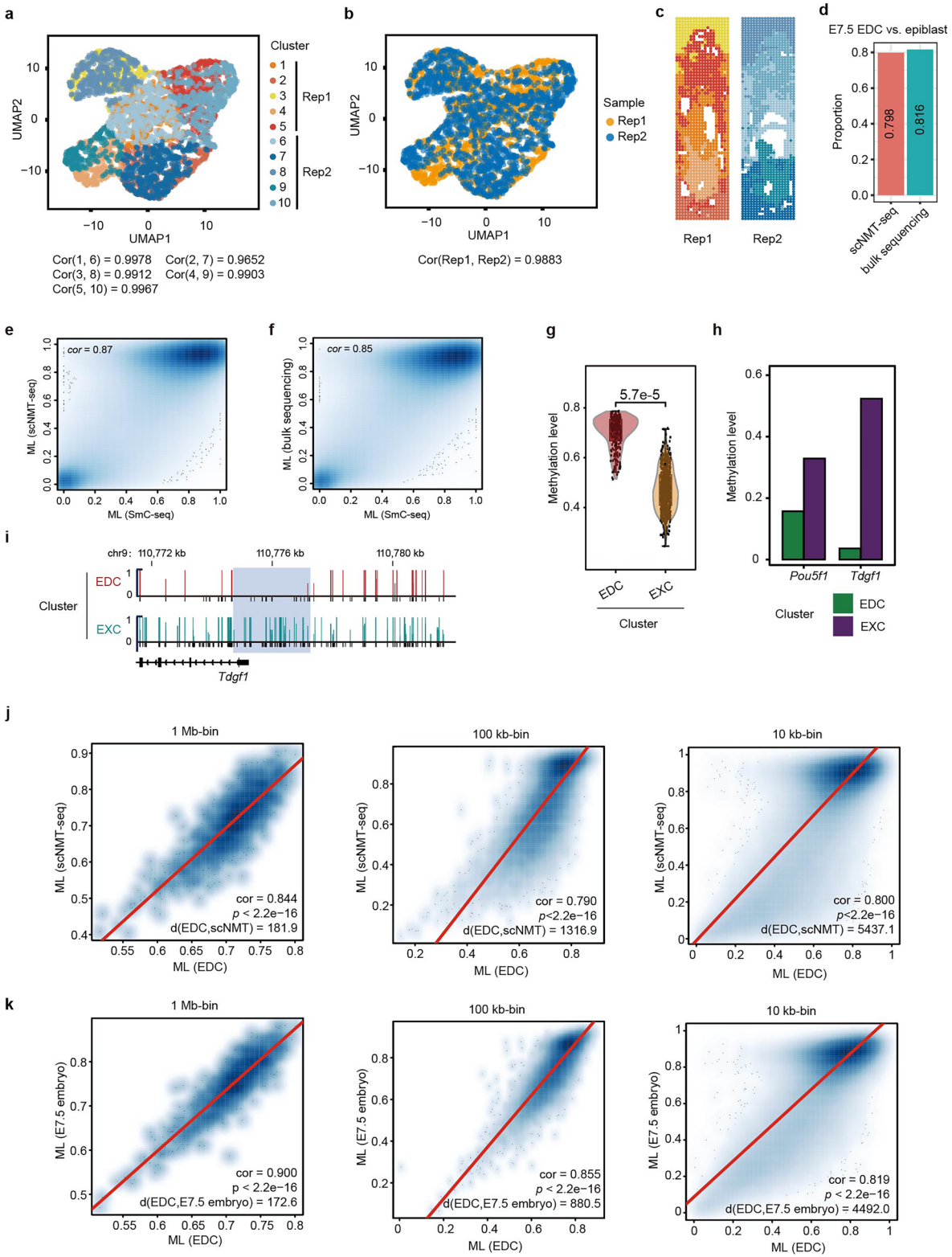

Extended Data Fig. 3 | See next page for caption.

https://doi.org/10.1038/s41592-026-03079-w

Extended Data Fig. 3 | Evaluation SmC-seq in E7.5 mouse embryo. a-b, UMAP visualization of SmC-seq data from two E7.5 embryo replicates, each at a 10 µm × 10 µm resolution, colored by clusters (**a**) or samples (**b**). The correlation coefficients are computed based on the global methylation levels of pixels for all overlapping cluster pairs in the UMAP plot (**a**) from different replicates. For example, Cor(3, 8) denotes the correlation coefficients between cluster 3 in replicate 1 and cluster 8 in replicate 2. The overall correlation coefficient between replicates (**b**) is then calculated as the mean of all such pairwise correlations. Cor, correlation coefficient; Rep, replicate. **c**, Spatial localization of distinct clusters (presented in **a**) within the corresponding E7.5 embryo section replicates. The colors refer to the clusters annotated in **a**. **d**, Proportion of 1 kb bins showing consistent methylation levels between SmC-seq data and other published data. The published data were obtained from Li *et al.*, (2023) and Argelaguet *et al.*, (2019). Two-sided Fisher's exact test was used. Bins that do not meet the criteria (BH-adjusted p value < 0.05 and methylation level difference ≥ 0.2) are considered to have consistent methylation levels. **e-f**, Scatter-plot comparing DNA methylation levels of non-overlapping 1 kb bins between EDC cluster from SmC-seq data and epiblast from public scNMT-seq data (**e**) or bulk sequencing data (**f**). **g**, Comparison of DNA methylation levels between EDC (n = 202) and EXC (n = 897) clusters in mouse E7.5 embryo. Two-sided wilcoxon rank-sum test was performed. EDC, epiblast-derived cell; EXC, extra-embryonic cell. Boxes denote the interquartile range (25th–75th percentiles), with the median marked inside. Whiskers extend to the furthest observations within 1.5 × IQR from the quartiles. **h**, DNA methylation levels of the promoters of well-known embryonic cell marker genes in EDC and EXC clusters. **i**, Genome browser view of pseudobulk DNA methylation levels at the *Tdgf1* promoter in EDC and EXC clusters. Light blue shadow marks the promoter of *Tdgf1*. The covered CpG sites in pseudobulk DNA methylation data are indicated below each track. **j**. Scatter plots comparing DNA methylation levels in non-overlapping bins of various sizes (1 Mb, 100 kb, 10 kb) between EDC cluster at the E7.5 stage measured by SmC-seq and E7.5 epiblast cells measured by scNMT-seq (Argelaguet *et al.*, 2019). Two-sided Pearson's product-moment correlation is used. Pearson's correlation coeffiecients (cor) and Euclidean distances (d) are shown. Linear regression lines are included. P value < 2.2e-16 indicates that the p value is smaller than the smallest positive floating-point number that can be represented by the computer. **k**, Scatter plots comparing DNA methylation levels in non-overlapping bins of various sizes (1 Mb, 100 kb, 10 kb) between EDC cluster measured by SmC-seq and E7.5 epiblast cells measured by bulk whole genome bisulfite sequencing (Li *et al.*, 2023). Two-sided Pearson's product-moment correlation is used. Pearson's correlation coeffiecients (cor) and Euclidean distances (d) are shown. Linear regression lines are included. P value < 2.2e-16 indicates that the p value is smaller than the smallest positive floating-point number that can be represented by the computer.

https://doi.org/10.1038/s41592-026-03079-w

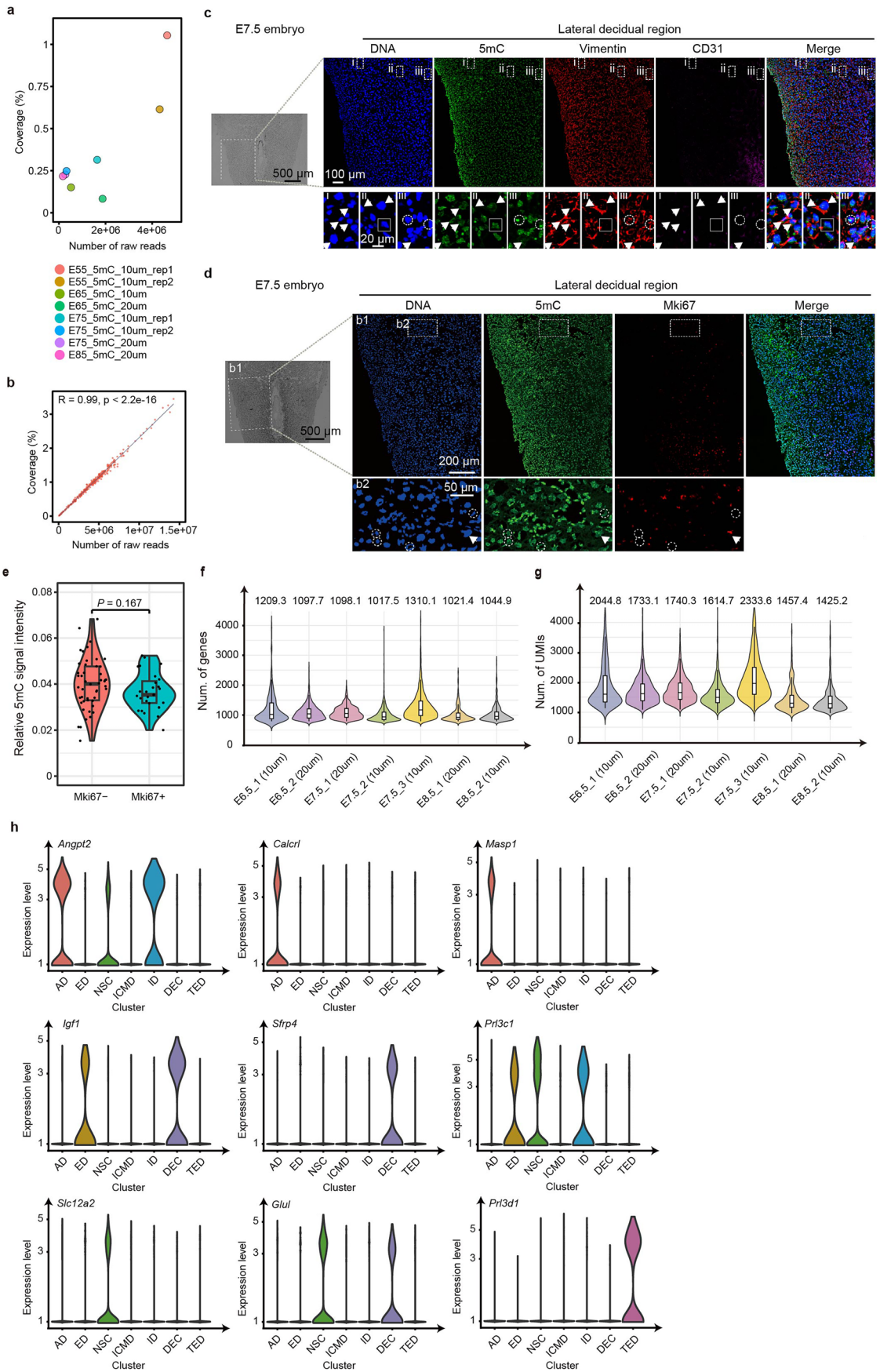

Extended Data Fig. 4 | See next page for caption.

https://doi.org/10.1038/s41592-026-03079-w

Extended Data Fig. 4 | Immunostaining and spatial transcriptomic profiling of E7.5 decidua. a. Scatter-plot showing the relationship between raw read counts and genome coverage across spatial 5mC datasets. **b**, Scatter-plot showing the relationship between raw read counts and genome coverage of an E5.5 sample. The solid line indicates the linear regression fits. R indicates Pearson's correlation coefficient. Two-sided t-test was used in this analysis. P value < 2.2e-16 indicates that the p value is smaller than the smallest positive floating-point number that can be represented by the computer. **c**, Immunostaining for 5mC, Vimentin and Cd31 in the lateral decidua at the E7.5 stage. Vimentin is a marker of stromal cell. Cd31 is a marker of endothelial cell. Arrows indicate stromal cells with low 5mC signal. Dashed circles indicate stromal cells with strong 5mC signal. Solid rectangles indicate a non-stromal cell with strong 5mC signal. Magnified views of regions i, ii, and iii are shown at the bottom. The data show that most of cells have positive staining of Vimentin, in contrast a small proportion of cells have positive staining of Cd31. The experiment was repeated independently 2 times with consistent results. **d**, Immunostaining for 5mC and Mki67 in the lateral decidua at the E7.5 stage. Arrows indicate stromal cells with low 5mC signal. Dashed circles indicate stromal cells with strong 5mC signal. Magnified views of the regions within the dashed rectangles are shown. **e**, Comparison of relative 5mC fluorescent signal intensities between $Mki67^{+}$ and $Mki67^{-}$ cells. The analysis was performed on the cells shown in the zoomed-in region in panel **d**. Wilcoxon rank-sum test was used. Boxes denote the interquartile range (25th–75th percentiles), with the median marked inside. Whiskers extend to the furthest observations within 1.5 × IQR from the quartiles. **f**, Violin plots showing the number of genes detected per pixel across different samples (number of pixels: E6.5_1 (10 μm), n = 891; E6.5_2 (20 μm), n = 2,045; E7.5_1 (20 μm), n = 3,324; E7.5_2 (10 μm), n = 2,601; E7.5_3 (10 μm), n = 7,333; E8.5_1 (20 μm), n = 1,257; E8.5_2 (10 μm), n = 1,610) in the spatial transcriptomic sequencing data. The widths of microchannel in fluidic chips used to generate corresponding data are indicated in parentheses. Boxes denote the interquartile range (25th–75th percentiles), with the median marked inside. Whiskers extend to the furthest observations within 1.5 × IQR from the quartiles. **g**, Violin plots showing the number of unique molecular identifiers (UMIs) detected per pixel across the same pixels as in **f**. Boxes denote the interquartile range (25th–75th percentiles), with the median marked inside. Whiskers extend to the furthest observations within 1.5 × IQR from the quartiles. **h**, Violin plots displaying the expression levels of representative marker genes across major clusters in embryo–uterus tissue, as detected by spatial transcriptomic sequencing. AD, angiogenic decidual cell; ED, endometrium; NSC, nutrient-supplier cell; ICMD, ICM-derived cell; ID, interface decidual cell; DEC, decidual endometrial cell; TED, TE-derived cell.

https://doi.org/10.1038/s41592-026-03079-w

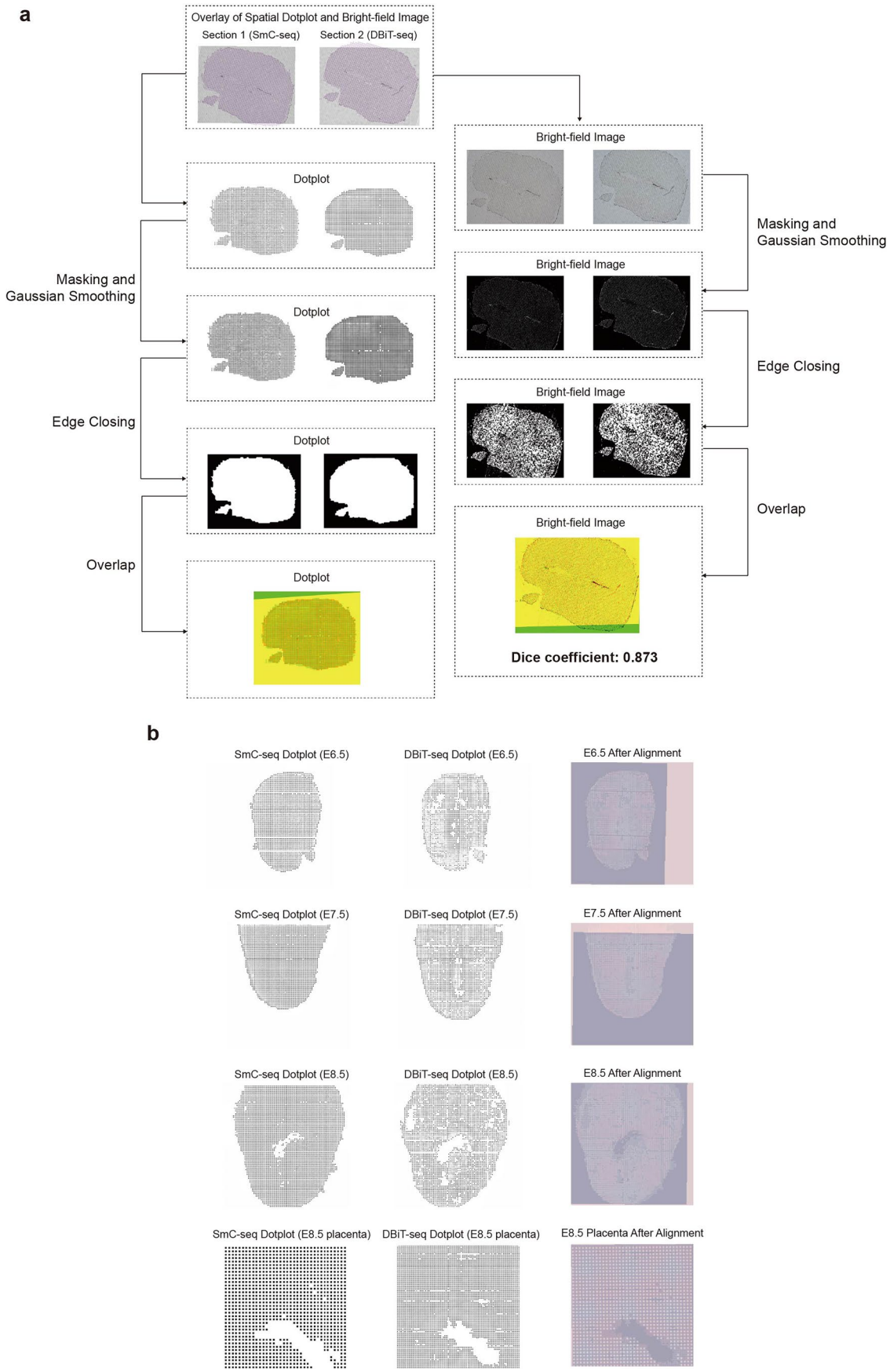

Extended Data Fig. 5 | See next page for caption.

https://doi.org/10.1038/s41592-026-03079-w

Extended Data Fig. 5 | Tissue outline-based integration of SmC-seq and spatial transcriptomic sequencing. a, Workflow and validation of data integration based on tissue outline, illustrated using adjacent E6.5 tissue sections. The top panel shows an overlay of the dot-plots and bright-field (BF) images, where each dot corresponds to a 10 µm-wide channel positioned over the tissue. The left panels illustrate the alignment workflow for dot-plots using the tissue outline as reference. The right panel shows alignment of the BF image to the same outline, serving as validation. After alignment, the Dice coefficient was calculated based on the original BF image to quantify registration accuracy. **b**, Integration results of SmC-seq and DBiT-seq data from E6.5, E7.5, and E8.5 stages, aligned based on tissue outlines.

https://doi.org/10.1038/s41592-026-03079-w

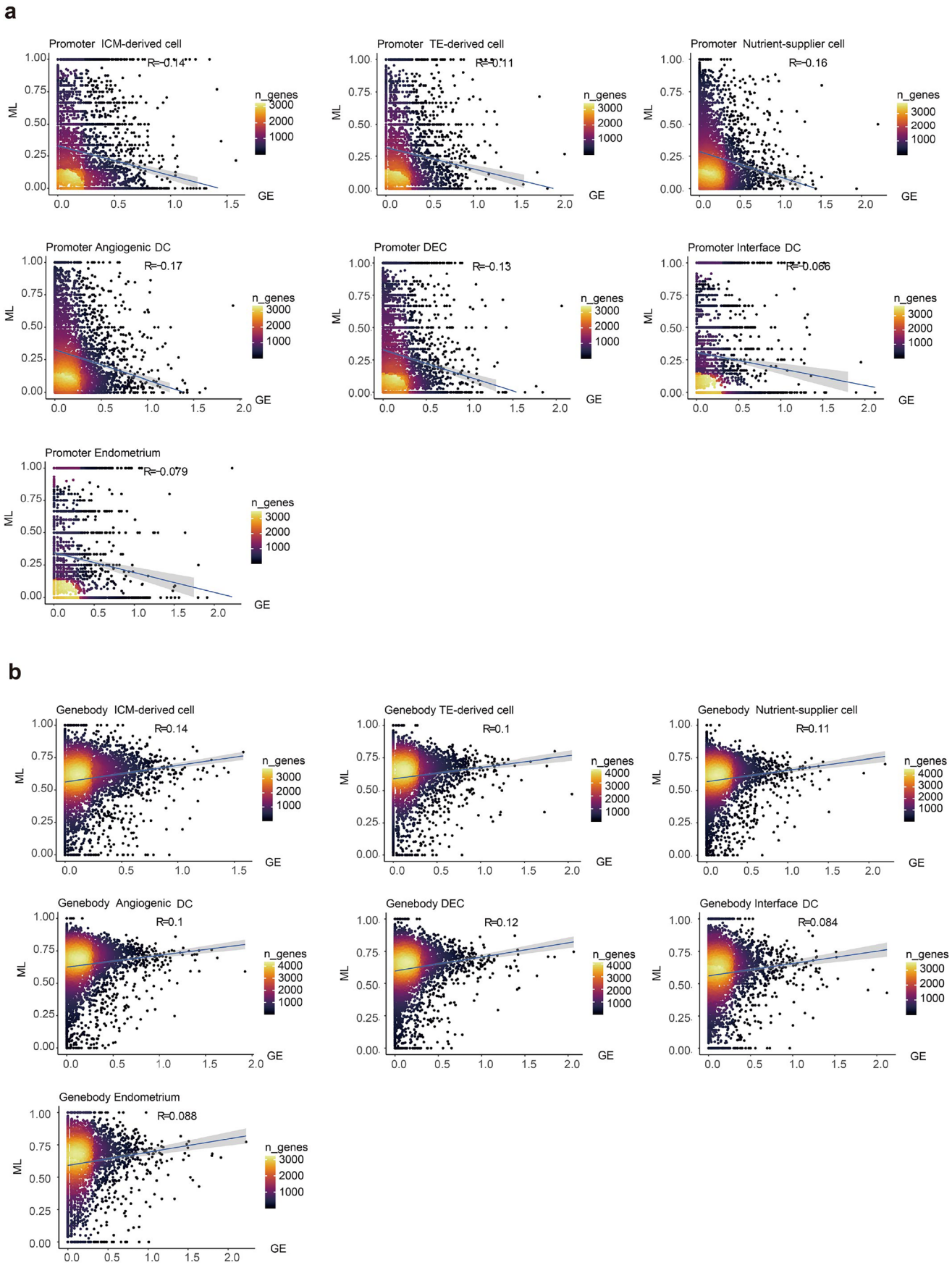

Extended Data Fig. 6 | See next page for caption.

https://doi.org/10.1038/s41592-026-03079-w

Extended Data Fig. 6 | Global correlation between DNA methylation and gene expression across major clusters in mouse embryo–uterus tissue. a, Density plot showing the correlation between DNA methylation levels at promoter regions and corresponding gene expression levels for all genes across distinct clusters. The clusters include ICM-derived cell cluster, TE-derived cell cluster, nutrient-supplier cell cluster, angiogenic DC cluster, DEC cluster, interface DC cluster, and endometrium cluster. The solid line denotes the linear regression fit and the shaded area the 95% confidence interval. R indicates Pearson's correlation coefficient. ML, methylation level; GE, gene expression; n_genes, number of genes. **b**, Density plot showing the correlation between gene body methylation levels and gene expression levels of all genes for the same clusters as in **a**. The solid line denotes the linear regression fit and the shaded area the 95% confidence interval. R indicates Pearson's correlation coefficient.

https://doi.org/10.1038/s41592-026-03079-w

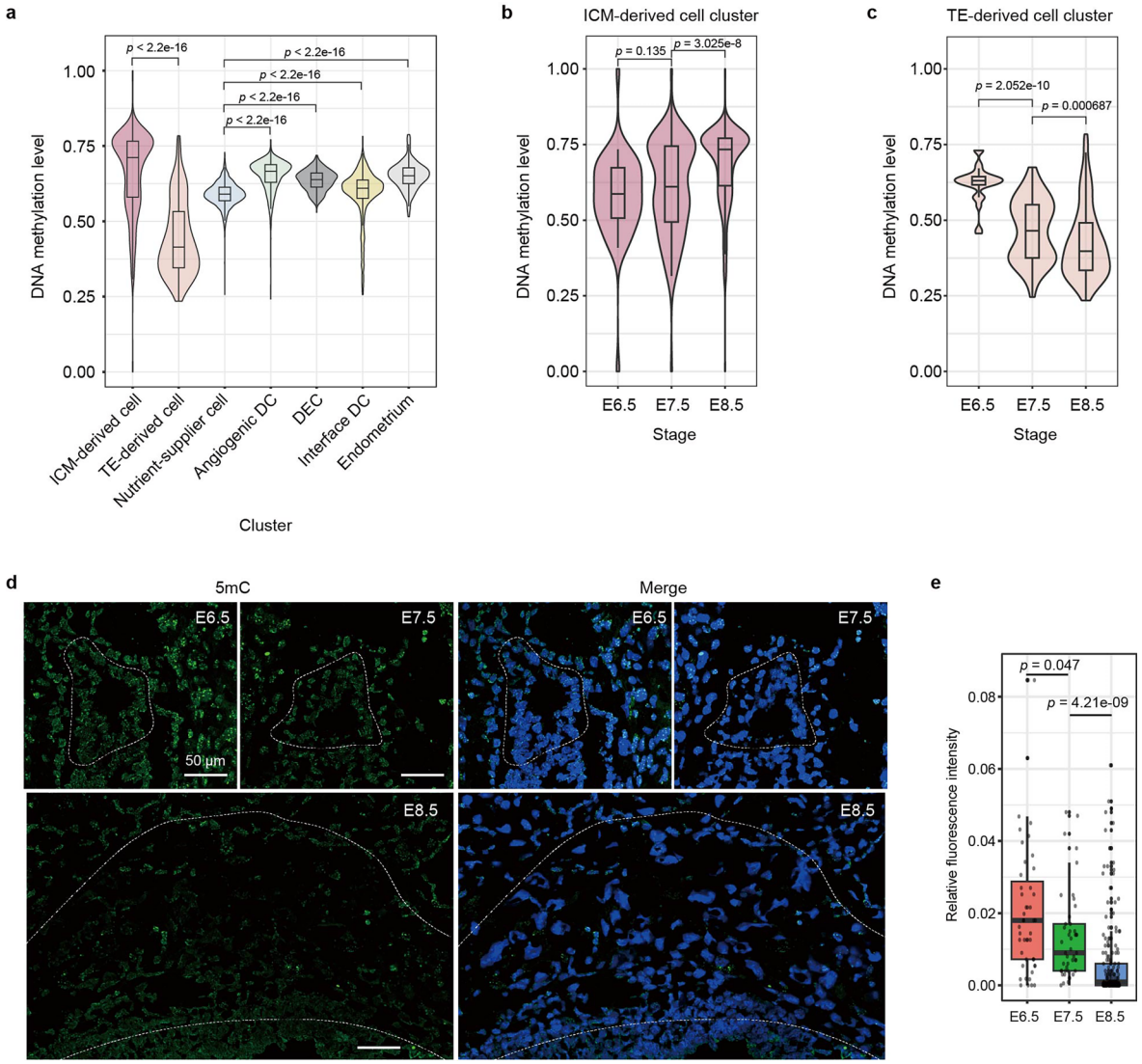

Extended Data Fig. 7 | DNA methylation levels across major clusters in mouse embryo–uterus tissue after implantation. a, DNA methylation levels of pixels in different clusters within mouse maternal-embryo tissues after implantation (ICM-derived cell, n = 615; TE-derived cell, n = 452; Nutrient-supplier cell, n = 3502; Angiogenic DC, n = 3183; DEC, n = 645; Interface DC, n = 843; Endometrium, n = 249). Two-sided wilcoxon rank-sum tests were used. Boxes denote the interquartile range (25th–75th percentiles), with the median marked inside. Whiskers extend to the furthest observations within 1.5 × IQR from the quartiles. P value < 2.2e-16 indicates that the p value is smaller than the smallest positive floating-point number that can be represented by the computer. ICM, inner cell mass; TE, trophectoderm; DC, decidual cell; DEC, decidual endometrial cell. **b-c**, Comparison of DNA methylation levels of pixels in ICM-derived cell cluster (E6.5, n = 43; E7.5, n = 116; E8.5 = 456) (**b**) and TE-derived cell cluster (E6.5, n = 28; E7.5, n = 76; E8.5 = 348) (**c**) among different developmental stages. Two-sided wilcoxon rank-sum tests were used. Boxes denote the interquartile range (25th–75th percentiles), with the median marked inside. Whiskers extend to the furthest observations within 1.5 × IQR from the quartiles. **d**, Immunostaining for 5mC in EPC from the E6.5 to E8.5 stages. Dashed circles mark the EPC regions. Scale bar, 50 μm. Blue color represent DNA signal (Hoechst 33342). **e**, Statistical results of relative 5mC fluorescence signal from the E6.5 to E8.5 stages (E6.5, n = 47; E7.5, n = 45; E8.5 = 189). Wilcoxon rank-sum test was used for statistical test. Boxes denote the interquartile range (25th–75th percentiles), with the median marked inside. Whiskers extend to the furthest observations within 1.5 × IQR from the quartiles.

https://doi.org/10.1038/s41592-026-03079-w

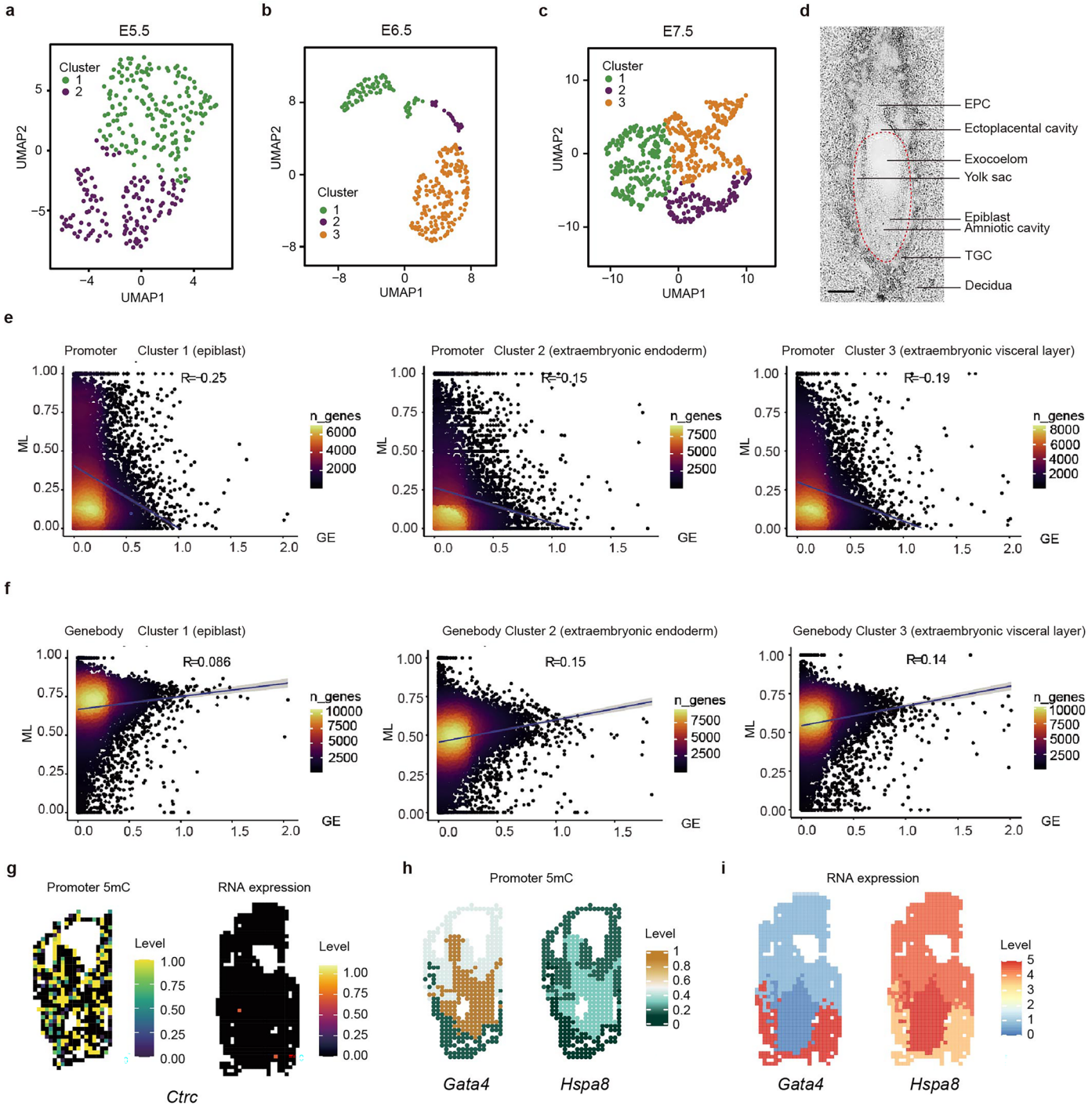

Extended Data Fig. 8 | Clustering and methylation-expression correlation of ICM-derived cells. a, UMAP visualization of clusters derived from the E5.5 ICM, classified based on SmC-seq data. Fluidic chips with 10 μm-width microchannels were used to generate the data. **b**, UMAP visualization of clusters derived from the E6.5 ICM, classified based on SmC-seq data. Fluidic chips with 10 μm-width microchannels were used to generate the data. **c**, UMAP visualization of clusters derived from the E7.5 ICM, classified based on SmC-seq data. Fluidic chips with 10 μm-width microchannels were used to generate the data. **d**, Bright-field images of a frozen section of E7.5 embryo. The tissue outlined by the red dashed line is derived from ICM. Scale bar, 200 μm. **e**, Density plot showing the correlation between DNA methylation levels at promoter regions and corresponding gene expression levels for all genes across different clusters. The solid line denotes the linear regression fit and the shaded area the 95% confidence interval. R indicates Pearson's correlation coefficient. Image generated from a single experiment. R, correlation coefficient; ML, methylation level; GE, gene expression; n_genes, number of genes. **f**, Density plot showing the correlation between gene body methylation levels and gene expression levels for all genes across the same clusters as in panel **e**. The solid line denotes the linear regression fit and the shaded area the 95% confidence interval. R indicates Pearson's correlation coefficient. **g**, Spatial distribution of promoter 5mC levels of *Ctrc* and its corresponding gene expression in an E7.5 embryo. Each pixel represents a 10 μm × 10 μm region. 5-μm-interval chips are used for this analysis. **h**, Spatial distribution of promoter 5mC levels of Gata4 and Hspa8 based on merged spatial 5mC data. **i**, Spatial distribution of average gene expression levels of Gata4 and Hspa8 across corresponding clusters shown in panel **h**.

https://doi.org/10.1038/s41592-026-03079-w

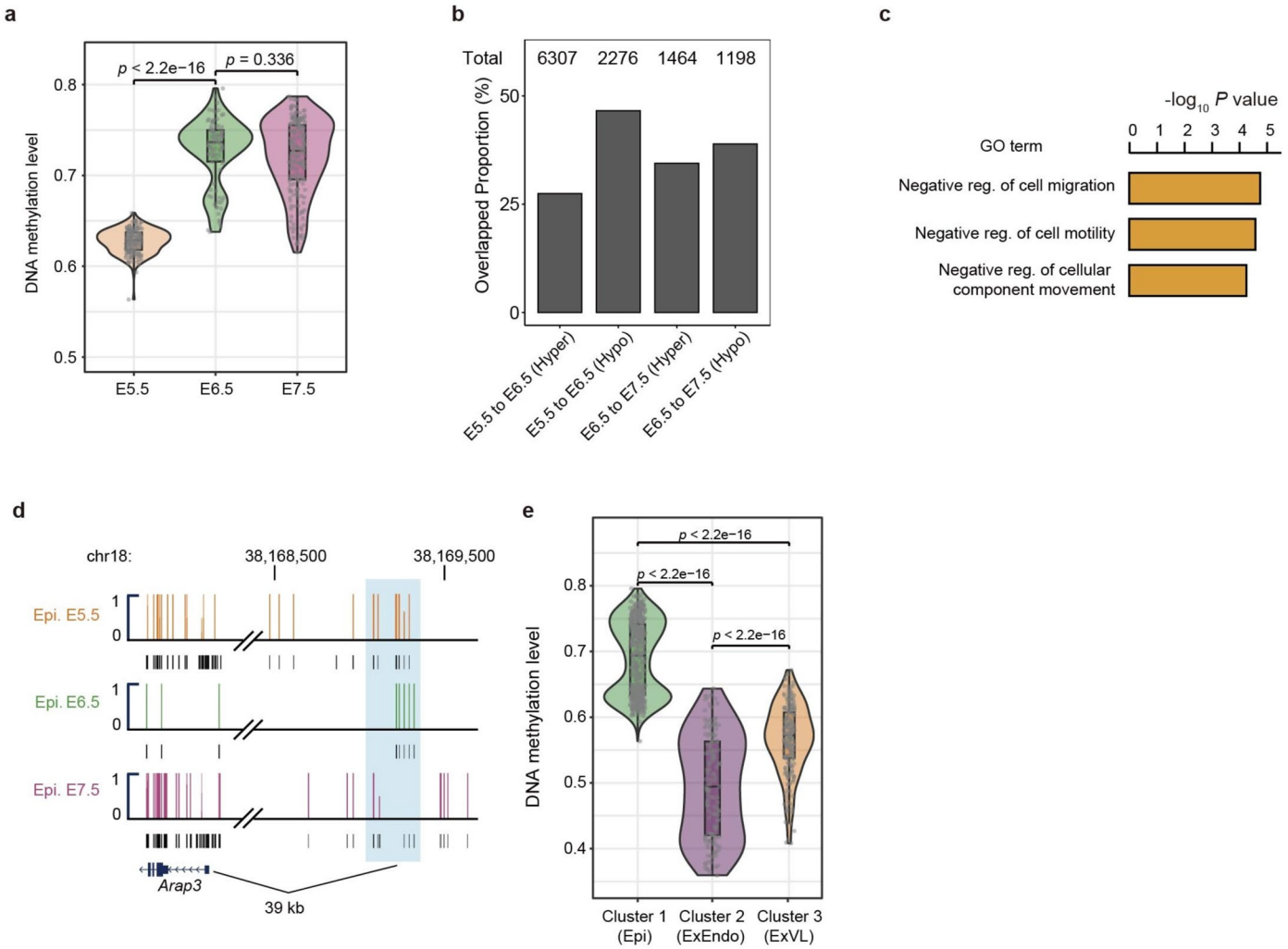

Extended Data Fig. 9 | DNA methylation dynamics and functional analysis in epiblast cluster across developmental stages. a, Comparison of DNA methylation levels of cluster 1 (epiblast) at different developmental stages (E5.5, n = 159; E6.5, n = 91; E7.5 = 202). Boxes denote the interquartile range (25th–75th percentiles), with the median marked inside. Whiskers extend to the furthest observations within 1.5 × IQR from the quartiles. P value < 2.2e-16 indicates that the p value is smaller than the smallest positive floating-point number that can be represented by the computer. **b**, Bar plot showing the percentages of hyperDMRs and hypoDMRs identified by SmC-seq that overlap with DMRs identified from published scNMT-seq data in mouse early embryo during gastrulation at the corresponding stages. The numbers of hyperDMRs and hypoDMRs detected by SmC-seq in epiblast cells from E5.5 to E7.5 stages are indicated above each bar. **c**, GO enrichment of genes associated with hypomethylated differentially methylated regions (hypoDMRs) in cluster 1 (epiblast) at the E7.5 stage compared to the E6.5 stage. reg., regulation. Enrichment analysis was performed using the GREAT web tool with a hypergeometric test. **d**, Genome browser view of DNA methylation levels of a hypoDMR in cluster 1 (epiblast) at the E7.5 stage that are associated with *Arap3*. Light blue shadow marks genomic region of the hypoDMR. Epi, epiblast. The methylation levels of the highlighted region at the E5.5, E6.5, and E7.5 stages, are 0.833, 1, and 0.333, respectively. **e**–**f**, Comparison of DNA methylation levels of pixels from different clusters at the E6.5 (Cluster 1, n = 91; Cluster 2, n = 28; Cluster 3 = 102) (**e**) and E7.5 (Cluster 1, n = 202; Cluster 2, n = 111; Cluster 3 = 209) (**f**) stages. Boxes denote the interquartile range (25th–75th percentiles), with the median marked inside. Whiskers extend to the furthest observations within 1.5 × IQR from the quartiles. P value < 2.2e-16 indicates that the p value is smaller than the smallest positive floating-point number that can be represented by the computer. ExEndo, extra-embryonic endoderm; ExVL, extra-embryonic visceral layer.

https://doi.org/10.1038/s41592-026-03079-w

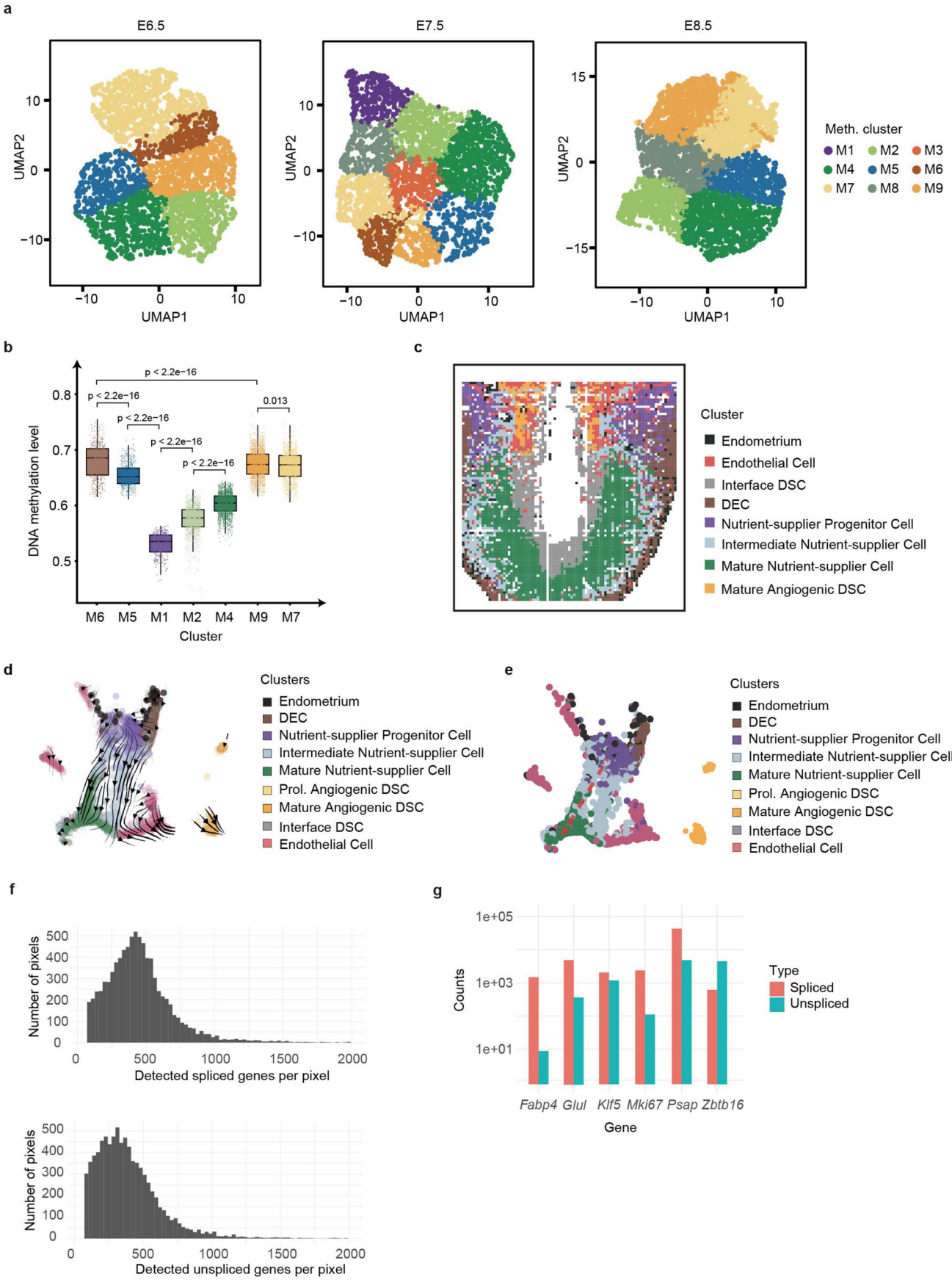

Extended Data Fig. 10 | See next page for caption.

https://doi.org/10.1038/s41592-026-03079-w

Extended Data Fig. 10 | Clustering, methylation dynamics, and spatial distribution of maternal decidua. a, UMAP visualization of clusters in maternal decidual tissues at different developmental stages, classified based on SmC-seq data. **b**, Comparison of DNA methylation level among clusters classified based on SmC-seq data of maternal decidual cells (M1, n = 264; M2, n = 1439; M4, n = 1837; M5, n = 563; M6, n = 355; M7, n = 1569; M9, n = 1300). The global DNA methylation of pixels was calculated. Boxes denote the interquartile range (25th–75th percentiles), with the median marked inside. Whiskers extend to the furthest observations within 1.5 × IQR from the quartiles. Two-sided wilcoxon rank-sum and signed rank tests were used. P value < 2.2e-16 indicates that the p value is smaller than the smallest positive floating-point number that can be represented by the computer. **c**, Spatial distribution of clusters in an E7.5 decidua at 10 μm × 10 μm resolution. **d**, RNA velocity analysis of spatial RNA-seq data from an E7.5 decidua section. Fluidic chips with 10 μm-width microchannels were used to generate the data. Each pixel represents a 10 μm × 10 μm region. **e**, UMAP visualization of spatial RNA-seq data from an E7.5 decidua section, with the inferred differentiation trajectory of nutrient-supplier cell lineage. The annotation of clusters is shown in panel **d**. **f**, Distribution of the number of detected spliced (top) and unspliced (bottom) genes per pixel in the dataset used for RNA velocity analysis. The x-axis shows the number of detected genes, and the y-axis shows the number of pixels. **g**, Total spliced and unspliced transcript counts across selected marker genes in the dataset used for RNA velocity analysis.

nature portfolio

Corresponding author(s): Jiang Liu, Lei Gao

Last updated by author(s): Jan 29, 2026

Reporting Summary

Nature Portfolio wishes to improve the reproducibility of the work that we publish. This form provides structure for consistency and transparency in reporting. For further information on Nature Portfolio policies, see our Editorial Policies and the Editorial Policy Checklist.

Statistics

For all statistical analyses, confirm that the following items are present in the figure legend, table legend, main text, or Methods section.

n/a	Confirmed
☐	☒ The exact sample size (*n*) for each experimental group/condition, given as a discrete number and unit of measurement
☐	☒ A statement on whether measurements were taken from distinct samples or whether the same sample was measured repeatedly
☐	☒ The statistical test(s) used AND whether they are one- or two-sided *Only common tests should be described solely by name; describe more complex techniques in the Methods section.*
☒	☐ A description of all covariates tested
☐	☒ A description of any assumptions or corrections, such as tests of normality and adjustment for multiple comparisons
☐	☒ A full description of the statistical parameters including central tendency (e.g. means) or other basic estimates (e.g. regression coefficient) AND variation (e.g. standard deviation) or associated estimates of uncertainty (e.g. confidence intervals)
☐	☒ For null hypothesis testing, the test statistic (e.g. *F*, *t*, *r*) with confidence intervals, effect sizes, degrees of freedom and *P* value noted *Give P values as exact values whenever suitable.*
☒	☐ For Bayesian analysis, information on the choice of priors and Markov chain Monte Carlo settings
☒	☐ For hierarchical and complex designs, identification of the appropriate level for tests and full reporting of outcomes
☐	☒ Estimates of effect sizes (e.g. Cohen's *d*, Pearson's *r*), indicating how they were calculated

Our web collection on statistics for biologists contains articles on many of the points above.

Software and code

Policy information about availability of computer code

Data collection	No software was used for data collection.
Data analysis	UMI-tools (version 1.1.2) was used to extract barcode information from the sequencing raw data. Trim Galore (version 0.6.6) was used to trim adapter sequences from sequencing reads. ST pipeline v1.7.238 was used for the read alignment and gene expression matrix calculation for RNA-seq data. Seurat v4.1.1 was used for RNA-seq data normalization, cell clustering, and cell type annotation. Bismark v0.23.0 was used for mapping and downstream analysis of SmC-seq data. The packages in R (v.4.2.3) were used in this study, including prcomp, stats, umap, clusterProfiler (v.4.6.2), enrichplot (v.1.18.4), org.Mm.eg.db (v.3.16.0), and biomaRt (v.2.54.1). ComplexHeatmap (v.2.14.0) was used for heat map plotting. No custom algorithms or software were used in this study. Code repository: https://github.com/LiuLab888/spatial-5mC-project

For manuscripts utilizing custom algorithms or software that are central to the research but not yet described in published literature, software must be made available to editors and reviewers. We strongly encourage code deposition in a community repository (e.g. GitHub). See the Nature Portfolio guidelines for submitting code & software for further information.

Data

Policy information about availability of data

All manuscripts must include a data availability statement. This statement should provide the following information, where applicable:

- Accession codes, unique identifiers, or web links for publicly available datasets
- A description of any restrictions on data availability
- For clinical datasets or third party data, please ensure that the statement adheres to our policy

The raw sequence data of SmC-seq and spatial RNA-seq reported in this paper have been deposited in the Genome Sequence Archive in National Genomics Data Center China National Center for Bioinformation (Accession number: CRA023723, CRA023723)

Research involving human participants, their data, or biological material

Policy information about studies with human participants or human data. See also policy information about sex, gender (identity/presentation), and sexual orientation and race, ethnicity and racism.

Reporting on sex and gender	No human participants are involved in this study.
Reporting on race, ethnicity, or other socially relevant groupings	No human participants are involved in this study.
Population characteristics	No human participants are involved in this study.
Recruitment	No human participants are involved in this study.
Ethics oversight	No human participants are involved in this study.

Note that full information on the approval of the study protocol must also be provided in the manuscript.

Field-specific reporting

Please select the one below that is the best fit for your research. If you are not sure, read the appropriate sections before making your selection.

☒ Life sciences ☐ Behavioural & social sciences ☐ Ecological, evolutionary & environmental sciences

For a reference copy of the document with all sections, see nature.com/documents/nr-reporting-summary-flat.pdf

Life sciences study design

All studies must disclose on these points even when the disclosure is negative.

Sample size	No sample-size calculation was performed. Two biological replicates were performed for samples at each developmental stage.
Data exclusions	No data were excluded from the analyses.
Replication	The distribution of 5mC levels should be comparable between two biological replicates of SmC-seq. The annotated cell types and the spatial distribution of these cells should be similar between the two biological replicates of spatial RNA-seq.
Randomization	The samples were randomly allocated into experimental groups.
Blinding	The investigators were blinded to group allocation.

Reporting for specific materials, systems and methods

We require information from authors about some types of materials, experimental systems and methods used in many studies. Here, indicate whether each material, system or method listed is relevant to your study. If you are not sure if a list item applies to your research, read the appropriate section before selecting a response.

Materials & experimental systems

n/a	Involved in the study
☐	☒ Antibodies
☒	☐ Eukaryotic cell lines
☒	☐ Palaeontology and archaeology
☐	☒ Animals and other organisms
☒	☐ Clinical data
☒	☐ Dual use research of concern
☒	☐ Plants

Methods

n/a	Involved in the study
☒	☐ ChIP-seq
☒	☐ Flow cytometry
☒	☐ MRI-based neuroimaging

Antibodies

Antibodies used: 5-methylcytosine antibody (Abcam, #ab10805, clone:33D3), Mki-67 antibody (Proteintech, #28074-1-AP), Vimentin antibody (Proteintech, #10366-1-AP), Alexa Fluor 647 anti-mouse CD31 antibody (Biolegend, #102415, clone: 390), Alexa Fluor 647 anti-Cytokeratin (pan reactive) Antibody (Biolegend, #628604, clone: C-11), Donkey anti-mouse IgG (H+L) highly cross-adsorbed secondary antibody, Alexa Fluo 488 (Invitrogen, #A-21202), Donkey anti-rabbit IgG (H+L) highly cross-adsorbed secondary antibody, Alexa Fluor 555 (Invitrogen, #A-31572).

Validation: All primary antibodies used in this study have been validated for immunostaining in mouse tissues, according to the information provided by the manufacturers. These antibodies have also been used in previously published studies. Detailed information is available on the manufacturers' websites.

Animals and other research organisms

Policy information about studies involving animals; ARRIVE guidelines recommended for reporting animal research, and Sex and Gender in Research

Laboratory animals: Wild-type C57BL/6N mice at 6-week old were used in this study. E5.5, E6.5, E7.5, and E8.5 mouse embryos were collected for SmC-seq and spatial-RNA sequencing.

Wild animals: Wild animals were not involved in this study.

Reporting on sex: The sex information of embryos was not collected.

Field-collected samples: The study did not involve samples collected from the field.

Ethics oversight: This study was approved by the Ethics Committee of the Institute of Biophysics, Chinese Academy of Sciences. The experimental procedures and animal care in this study were carried out in accordance with the guidelines set by the Institutional Animal Care and Use Committee (IACUC) the Institutional Committee on Biosafety & Experimental Animal Management at the Institute of Biophysics, Chinese Academy of Sciences.

Note that full information on the approval of the study protocol must also be provided in the manuscript.

Plants

Seed stocks: Plants are not involved in this study.

Novel plant genotypes: Plants are not involved in this study.

Authentication: Plants are not involved in this study.